Retrogressed lawsonite blueschists from the NW Iberian Massif: P–T–t constraints from thermodynamic modelling and $^{40}Ar/^{39}Ar$ geochronology

Alicia López-Carmona · Jacobo Abati · Pavel Pitra · James K. W. Lee

A. López-Carmona (✉) · J. Abati
Departamento de Petrología y Geoquímica (UCM),
Instituto de Geociencias (IGEO-CSIC), 28040 Madrid, Spain
e-mail: alcarmona@geo.ucm.es

A. López-Carmona · P. Pitra
Géosciences Rennes, UMR 6118, Université Rennes 1
and CNRS, 35042 Rennes Cedex, France

J. K. W. Lee
Department of Earth and Planetary Sciences,
Macquarie University, North Ryde, NSW 2109, Australia

Abstract Blueschist facies terranes in the Variscan Ibero-Armorican Arc are restricted to scarce and relatively small areas. One of these examples is the Cea´n Unit, which is the westernmost exposure of the middle allochthonous sheet of the Variscan belt in the Malpica–Tui Complex (NW Ibe-rian Massif). The Cea´n Unit is a highly condensed meta-morphic succession with a lower part in the blueschist facies and an upper part without HP relicts. It comprises variable proportions of glaucophane–chloritoid-bearing metapelites and mafic rocks with abundant well-preserved pseudomorphs after euhedral lawsonite. Both lithologies show systematic changes in texture and mineral composi-tion that are spatially related depending on deformation. The metamorphic evolution of the metabasic rocks has been constrained in the *P–T* space through pseudosection approach and is characterised by H_2O-undersaturated pro-grade evolution induced by the crystallisation of lawsonite. Peak conditions in the blueschist/LT-eclogite facies have been constrained at ca. 2.2 GPa and 560 °C. Exhumation-related metamorphism is characterised by a nearly iso-thermal decompression from the lawsonite-bearing fields to fields with stable albite at $P \approx 1$ GPa. This lead to the pseudomorphism of lawsonite in the early-decompression stages, and a subsequent amphibolite–greenschist facies overprint at $P < 0.8$ GPa and $T \approx 440$–480 °C. The preservation of the lawsonite crystal shape despite com-plete retrogression indicates that pseudomorphism occurred as a static process and that particular levels of the blue-schist host rock were not affected by penetrative defor mation during exhumation. $Ar/^{39}Ar^{40}$ step heating of phengitic muscovite from the pelitic schists interbedded with the lawsonite pseudomorph-bearing metabasic rocks yield plateau ages of ca. 363 ± 2 and 354 ± 1 Ma. The older age is interpreted as the age of the peak blueschist facies metamorphism. The age of 355 Ma is interpreted as a cooling age and is inferred to represent some point rel-atively close to peak conditions at the onset of the iso- thermal decompression. $Ar/^{39}Ar^{40}$ dating of muscovite from the quartzo-feldspathic mylonites of the Bembibre–Cea´n detachment, at the base of the Cea´n Unit, yields an age of ca. 337 ± 3 Ma, interpreted as the age of the post-nappe extensional tectonics. Similar data obtained from the blueschists of Ile de Groix (Armorican Massif; Bosse et al. in Chem Geol 220:21–45, 2005) support the equivalence of the Cea´n Unit and the Upper Unit of Ile de Groix along the Ibero-Armorican Arc and suggest that these units share a blueschist facies event constrained at ca. 360–370 Ma, that is inferred to represent the Late Devonian–Early Carbon-iferous subduction of the northern margin of Gonwana beneath Laurussia.

Keywords Lawsonite blueschist · Pseudomorphs after lawsonite · H_2O · Ibero-Armorican Arc

Introduction

The Malpica–Tui Complex (MTC; Fig. 1) is located in the NW section of the Iberian Massif, constituting the westernmost outcrop of the internal areas of the European Variscan Belt. The MTC can be separated in two tectonically juxtaposed sequences with different tectonometamorphic evolution: (1) a lower sequence, the so called Malpica–Tui Unit (MTU), dominated by felsic orthogneisses and turbiditic metasedimentary rocks and (2) an upper sequence, the so called Cea´n Unit, that comprises metasediments intercalated with MORB-type metavolcanic rocks (Arps 1981). They correspond, respectively, to the lower and middle allochthon of the Variscan nappe stack in the Ibero-Armorican Arc (IAA; Balle`vre et al. in press). Peak metamorphic conditions in the MTU are in the intermediate temperature eclogite facies (P & 25 kbar and T & 610 □C; Rodrı´guez Aller 2005) and have been constrained at ca. 370 Ma by U–Pb on zircon (Abati et al. 2010). On the other hand, peak conditions in the Cea´n Unit are in the blueschist facies conditions (Rodrı´guez Aller 2005; L ó pez-Carmona et al. 2010, 2013), and the HP event is constrained by a single $^{40}Ar/^{39}Ar$ age on muscovite of 348 ± 8 Ma (Rodrı´guez Aller et al. 2003). Pseudomorphs after lawsonite were first reported by Rodrı´guez Aller et al.(2003) in the metabasic rocks of the Cea´n Unit. However, a detailed petrographic and thermobarometric study of these rocks has never been done and constitutes the main objective of this research. In order to understand the tec-tonic evolution and the apparent metamorphic zoning of the MTC, particular attention is paid to the relations of the metamorphic assemblages with the deformational fabrics. Preliminary studies on the metabasic rocks using conven-tional thermobarometric technics suggest peak conditions in the epidote–blueschist facies (minimum P = 1.4–1.8 GPa and T = 440–525 □C; Rodrı´guez Aller 2005).

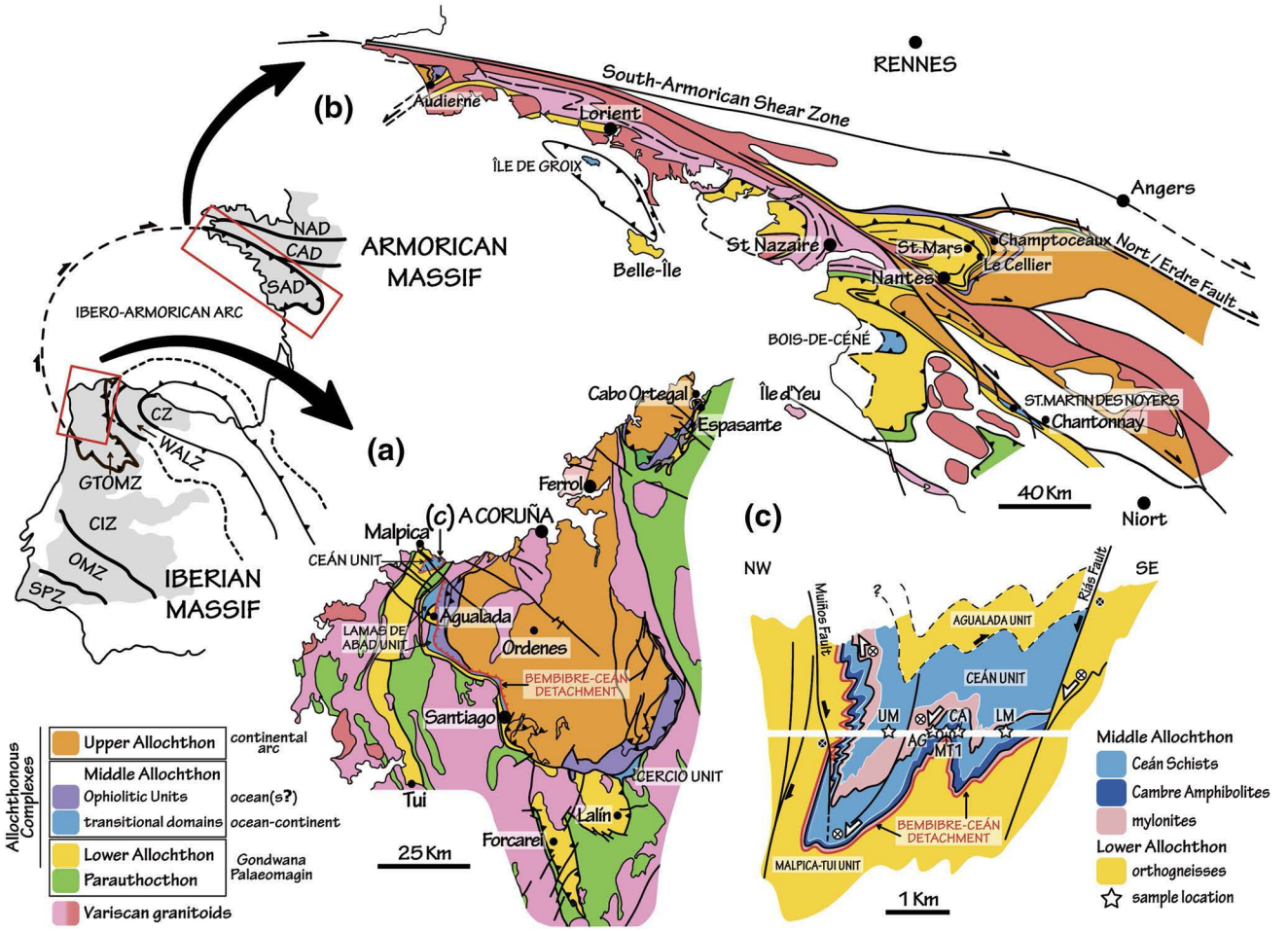

Fig. 1 Location of the Ibero-Armorican Arc in the Variscan orogen. Geological map of the allochthonous units in the a NW Iberian Massif and in the b South Armorican Domain. c Cross-section for the middle allochthon in the Malpica–Tui Complex. The stars indicate sample location. CZ Cantabrian Zone, WALZ West Asturoccidental-leonese Zone, GTOMZ Galicia-Tras-os-Montes Zone, CIZ Central Iberian Zone, OMZ Ossa-Morena Zone, SPZ South Portuguese Zone, NAD North Armorican Domain, CAD Central Armorican Domain, SAD South Armorican Domain. Modified from Balle`vre et al. (2009), Martı´nez Catala´n et al. (2009) and Balle´vre et al. (in press)

Thermodynamic modelling of phase equilibrium in the interbedded metasediments indicates that this sequence developed a metamorphism in the blueschist facies conditions constrained at ca. 1.9–2.2 GPa, 460–520 ° C (Lo ´pez-Carmona et al. 2013). Studying the *P–T* evolution of the retrogressed lawsonite pseudomorph-bearing metabasic rocks through pseudosection approach aims to establish the tectonothermal evolution for the Cea´n Unit in the MTC. The contact between the upper and the lower sequences of the MTC (i.e. between the lower and the middle allochthon) is marked by a several metres thick layer of mylonites and ultramylonites located at the base of the metabasic rocks known as the Bembibre–Ceán Detachment. This detachment is part of the Bembibre–Pico Sacro detachment system (formed by the Bembibre–Ceán and the Pico Sacro detachments; see Gómez Barreiro et al. 2010 and Díez Fernández et al. 2012) and resulted from a regional-scale extensional episode that reactivated pre-existing tectonic contacts. It is thought to be coeval with late orogenic collapse and widespread magmatism, representing its upper crustal expression (cf. Gómez Barreiro et al. 2010; Díez Fernández et al. 2012). However, its precise age remains unconstrained. Dating the formation of this mylonite and the blueschist facies fabric in the Ceán Unit by $^{40}Ar/^{39}Ar$ step heating constitutes the second purpose of this study. Considering the above objectives, an attempt to establish possible equivalences between the lower and middle allochthons in the MTC and similar terranes in the southern Armorican Massif, along the IAA, will be carried out.

Table 1 (a) Bulk-rock composition from XRF analyses of sample CM expressed in wt% and normalised in mol.% to the NCKFMASHTO chemical system. (b) Bulk-rock compositions normalised with THERMOCALC expressed in mol.%

(a)	wt%	mol.%	(b)	NCKFMASHTO (mol.%)			
SiO_2	47.89	53.28	SiO_2	53.28	53.28	48.66	47.87
TiO_2	1.92	1.60	TiO_2	1.60	1.60	1.47	1.44
Al_2O_3	13.36	8.76	Al_2O_3	8.76	8.76	8.00	7.87
FeO	8.49	7.90	FeO	7.90	7.90	7.22	7.10
$Fe_2O_3^a$	4.20	1.76	O	1.75	1.75	0–2*O	1.62
MnO	0.22		MgO	11.79	11.79	10.77	10.59
MgO	7.11	11.79	CaO	11.71	11.71	10.70	10.53
CaO	10	11.72	Na_2O	3.15	3.15	2.88	2.83
Na_2O	2.92	3.15	K_2O	0.04	0.04	0.04	0.04
K_2O	0.07	0.05	H_2O	*in excess*	0–25	10.27	10.11
P_2O_5	0.13		Figure	9a	9b	9c	9d

[a] $Fe_2O_{3(T)}$ was measured by the XRF and FeO by wet chemical titration. The amount of Fe_2O_3 is calculated stoichiometrically as: [total iron/1.43 − (FeO/1.286)*1.43]

Retrogressed blueschists: the Cambre metabasic rocks

The Cambre metabasic rocks (Llana-Fúnez 2001; Rodríguez Aller 2005) are intensely foliated amphibolites and greenschists with N-MORB chemical composition (Table 1) (Arps 1981; González Lodeiro et al. 1984; Rodríguez Aller 2005). They outcrop in the upper structural levels of the MTC, at the base of the Pazos Synform, and together with the pelitic schists constitute the Ceán Unit (Fig. 1c). The Cambre metabasic rocks immediately overlie the so-called Bembibre–Ceán detachment, which marks the limit between the lower and the middle allochthon in the MTC (Díez Fernández et al. 2011; Fig. 1a, b; Fig. 1a of ESM). The dominant rock type is teal/bluish-green fine- to medium-grained garnet-bearing amphibolite with frequent levels containing pseudomorphs after lawsonite. At the base of the sequence, the metabasic rocks are interbedded with chloritoid–glaucophane-bearing metapelites (Fig. 1b, c of ESM) (López-Carmona et al. 2010, 2013). The lawsonite pseudomorph-bearing amphibolite levels are <10 m thick (Fig. 1d, f of ESM). Going upwards in the sequence, lawsonite pseudomorphs disappear gradually, over a short vertical distance, and amphibolites grade into greenschists with garnet porphyroblasts dispersed in a dark green matrix (Fig. 1g, i of ESM). The greenschists contain epidote-rich layers several centimetres up to 1–2 m thick (Fig. 1h of ESM). Finally, the top of the succession is dominated by greenschists with albite porphyroblasts ("prasinites") (Rodríguez Aller 2005; Fig. 1j of ESM) and fine-grained pelitic schists without garnet (Fig. 1k of ESM).

Deformation history

Deformation in the Cambre metabasic rocks is highly heterogeneous. Whereas in some levels, the lawsonite pseudomorphs preserve the euhedral shape (Fig. 2a-1), and towards the top of the sequence, the pseudomorphs are strongly stretched and almost indistinguishable from the matrix (Fig. 2a-2). Mylonitic to ultra-mylonitic layers are localised in the basal part, at the contact with the gneisses of the lower allochthon, along the Bembibre–Ceán detachment (Fig. 1a, b, Fig. 1a of ESM). However, deformation history in the Cambre metabasic rocks would include several compressive, extensional and strike-slip phases (Díez Fernández et al. 2011).

Three foliations, with uneven development at different structural levels, have been identified. The main foliation in the lower part of the sequence is defined by the shape-preferred orientation of amphibole, epidote, albite, chorite and muscovite. This foliation wraps gently around mostly euhedral crystals of garnet and lozenge-shaped aggregates containing epidote, chlorite, albite and white micas, interpreted as pseudomorphs after lawsonite (Fig. 2a-1, b; cf.

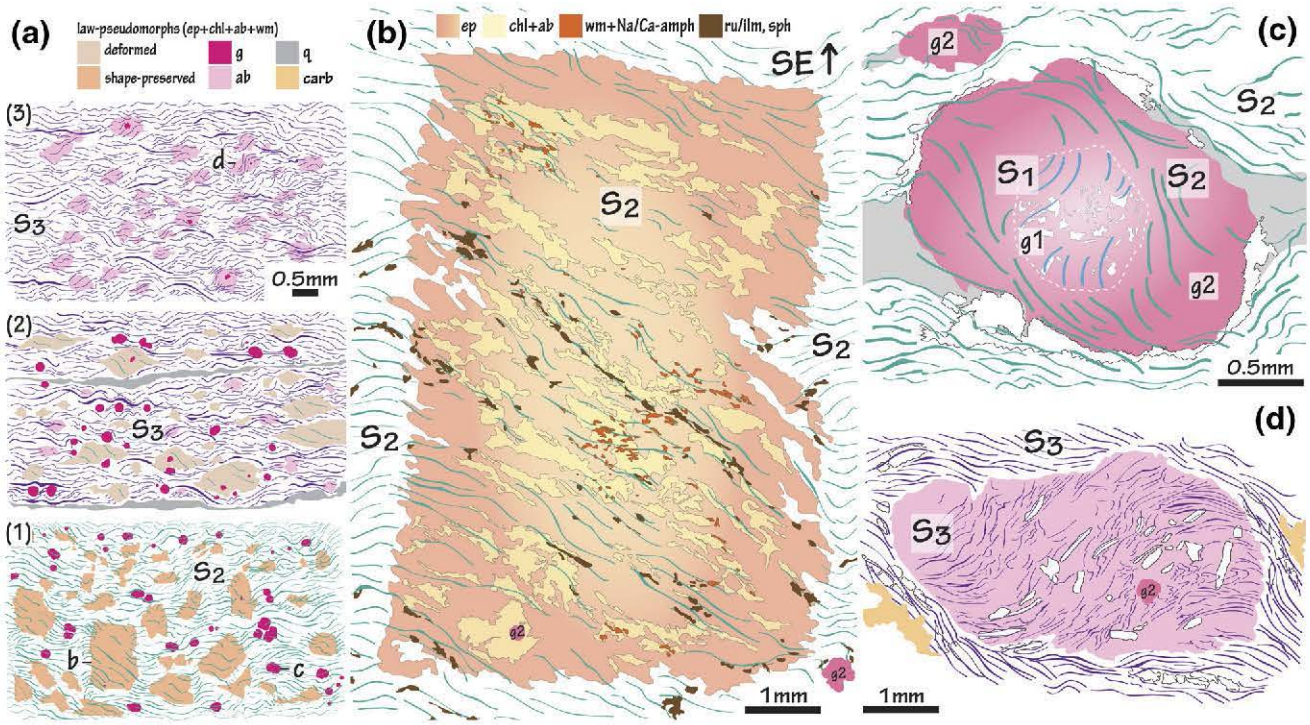

Fig. 2 Schematic illustration highlighting foliations **a** at different structural levels of the sequence, from the bottom (*1*) to top (*3*) of the series; **b** in lawsonite pseudomorphs; **c** in garnet porphyroblasts; **d** in albite porphyroblasts. Mineral abbreviations are after Holland and Powell (1998). *carb* carbonates, *g1* garnet 1, *g2* garnet 2, *Na/Ca-amph* sodic/calcic amphiboles, *wm* white mica

Ballèvre et al. 2003; Rodríguez Aller et al. 2003). Unoriented, or partially oriented, relicts of an early assemblage preserved in the core of garnet porphyroblasts are related to an incipient foliation S_1. A second foliation, S_2, develops in the garnet rim and is continuous with the matrix foliation, suggesting syntectonic growth of garnet (Fig. 2c). Pseudomorphs after lawsonite comprise oriented crystals of epidote and stretched clusters interpreted as inclusions in the original lawsonite crystals. Stretched clusters define a slightly curved internal foliation, generally oblique to but continuous with the matrix foliation (Fig. 2b), suggesting that the crystallisation of lawsonite is also contemporaneous with the development of S_2. Clusters are composed of rutile/ilmenite and titanite and of chlorite–albite aggregates. Their mineralogy indicates that chlorite–albite aggregates may represent pseudomorphs after a former phase, most likely, glaucophane (cf. Le Bayon et al. 2006; Rodríguez Aller 2005). The preservation of the euhedral shape of the former lawsonite crystals suggests that pseudomorphism occurred as a static process, and these rocks were not affected by any further ductile deformation (cf. Ballèvre et al. 2003; Philippon et al. 2013). To the top of the succession, the main foliation is defined by the shape-preferred orientation of amphibole, epidote, chlorite, albite and minor amounts of muscovite, and is parallel to boudined layers of quartz and, locally, epidote. This foliation, S_3, wraps around garnet and strongly deformed pseudomorphs after lawsonite (Fig. 2a-2). In intensely deformed samples, lawsonite pseudomorphs are absent and porphyroblasts of albite dominate. Albites contain anhedral crystals of garnet and sigmoidal inclusion trails, continuous with the matrix foliation, suggesting the syntectonic growth of albite (Fig. 2a-3, d). The development of S_3 is limited to the upper part of the sequence. Thus, the associated deformation was concentrated at this structural level. However, this foliation reworks S_2, as evidenced by the relics in lawsonite pseudomorphs and garnet inclusions in albite porphyroblasts.

Petrography and mineral chemistry

Two representative samples of the Cambre metabasic rocks have been chosen for a detailed study. Sample 106343, referred to hereafter as CA (for Cambre Amphibolites), is located in the intermediate part of the sequence. The presence of numerous garnet porphyroblasts, rich in S_1 and S_2 inclusions, and the abundant well-preserved pseudomorphs of ehuedral lawsonite, makes this sample ideal to study the early-deformation phases. Additionally, textural and chemical relations have been investigated in similar samples located at equivalent levels, and some of the petrographic images correspond to such examples (samples 109952 and 109954). Sample 106331, referred to hereafter

as AG (for Albite Greenschists), represent albite-bearing samples located at the top of the succession. The occurrence of syn-S_3 albite porphyroblasts allows investigating the late exhumation-related stage. Analytical details, mineral abbreviations and compositional variables are described in the "additional information" file, provided as electronic supplementary material.

Sample CA

In sample CA, calcic to sodic-calcic amphiboles constitute up to 80 % in volume of each sample (determined by point counting) and define the main foliation S_2. Other matrix minerals are, in the order of decreasing abundance, epidote, chlorite, albite, phengitic muscovite, titanite, rutile/ilmenite, magnetite, haematite, apatite and quartz (Fig. 3; Table 2 of ESM). Chlorite (type 2), nearly pure albite (type 2), titanite (type 2b) and rutile partially or almost completely replaced by ilmenite (type 2; Fig. 2a of ESM) are relatively homogeneous, whereas epidote is strongly zoned (type 2b; Table 2 of ESM). Phengitic muscovite (type 2) has Si contents ranging typically between 3.38 and 3.42 pfu, reaching a maximum value of 3.46. In the most deformed areas, the Si contents are systematically lower.

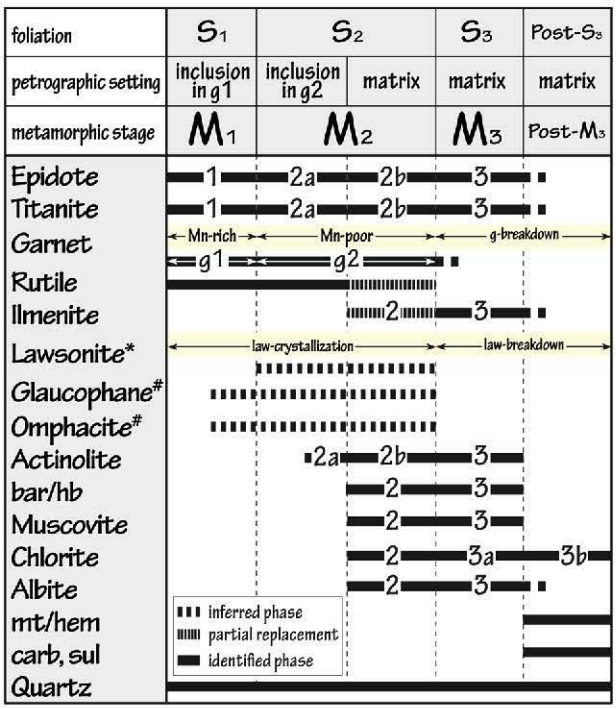

Fig. 3 Diagram showing the crystallisation–deformation relations of the Cambre metabasic rocks. "*asterisk*" specifies phases inferred from petrography and/or from petrologic modelling that have not been identified petrographically. "#" indicates phases described by other authors that have not been recognised in this study

Amphiboles in the matrix

Calcic amphiboles are fine- to medium-grained (0.025–0.3 mm) and are either actinolite (pale green hue; type 2a) with hornblende rims (green-bluish) or slightly zoned hornblende crystals (blue-green to deep green; type 2). Coexisting actinolite and hornblende are commonly found together in a patchy intergrowth. Large domains in the matrix foliation consist of very fine-grained symplectitic intergrowth of hornblende (commonly with actinolite cores) and albite (Fig. 2b, c of ESM). Rodríguez Aller (2005) described omphacite as very rare pre-S_3 prisms, showing irregular rims of hornblende–albite symplectites. Relicts of omphacite have not been identified in the samples of this study. However, the hornblende–albite symplectitic intergrowth possibly represents replacement of former crystals of omphacitic pyroxene (e.g. Miller et al. 1980; Ortega-Gutiérrez et al. 2004; Vega-Granillo et al. 2007; López-Carmona et al. 2011) or glaucophanic amphibole (e.g. Miller et al. 1980; Liou 1981; Engvik et al. 2000). The general zonation trend in amphiboles, from core-to-rim, is characterised by a decrease in Ca and an increase in Na, Al, Fe^{3+} and the X_{Fe} ratio (Table 2 of ESM). In all amphiboles, K and Ti proportions are always close to zero and the X_{Fe} ratio is below 0.5. In all analyses, Ca_{M4} is systematically higher than total Na, and a continuous range of compositions between actinolite and hornblende sensu lato is observed, the former being closer to calcic compositions, and the latter tending towards calcic-sodic compositions (Fig. 4). Only in a limited number of analyses Na_B (=Na_{M4}) >0.5. These sodic-calcic amphiboles are small (<0.1 mm) single prismatic to subhedral crystals of barroisitic hornblende (type 2; Table 2 of ESM).

Garnet zoning and inclusion patterns

Garnet forms subhedral to ehuedral porphyroblasts (up to 2.5 mm in diameter) that commonly display optical zoning. The cores of the porphyroblasts, referred to as garnet 1 (g1), contain very fine-grained inclusions of epidote (type 1; 5–10 μm), titanite (type 1), very tiny rutile needles (<2 μm) and quartz (Figs. 3, 5b; Table 3 of ESM). The inclusions define a subtle internal foliation (S_1) that has unoriented or curved patterns. In the outer part of the garnet porphyroblasts (referred here to as garnet 2, g2), S_1 turns progressively continuous towards another internal foliation (S_2), which is continuous with the matrix foliation (S_2; Fig. 2c). S_2 is formed by slightly coarser-grained inclusions (0.01–0.2 mm) of epidote (type 2a), titanite (type 2a), very small crystals of rutile partially replaced by ilmenite (<4 μm), amphibole and quartz. Amphiboles form subhedral crystals of unzoned actinolite (<150 μm; type 2a; Fig. 5b; Table 3 of ESM). Additionally, single grains

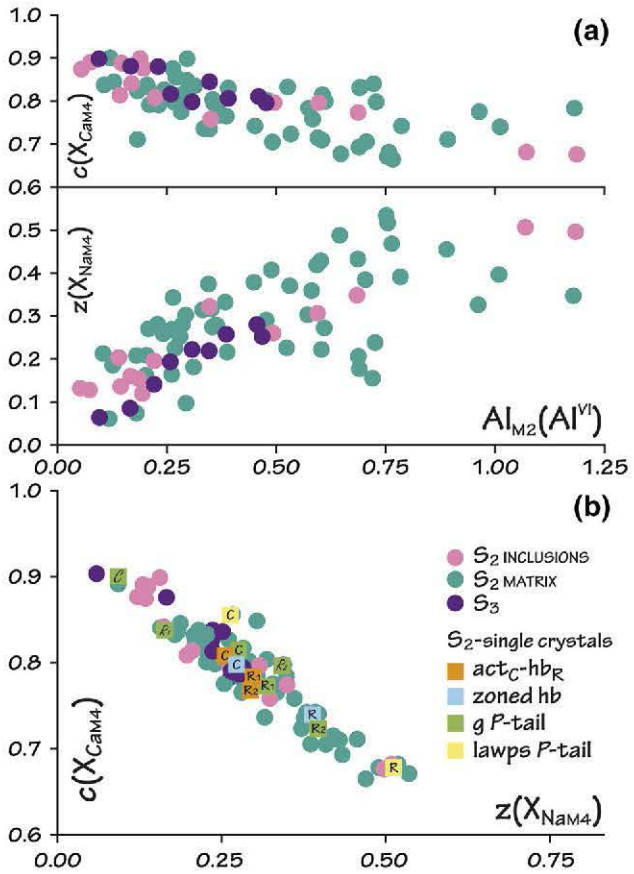

Fig. 4 Compositional variations in amphiboles in the Cambre metabasic rocks. *C* core, *R* rim, *P-tail* crystallisation tail, *lawps* lawsonite pseudomorph. Mineral abbreviations are after Holland and Powell (1998)

of actinolite (type 2a) showing exsolution lamellae of hornblende are preserved in the outermost rims of some garnets (Fig. 2f of ESM, Fig. 5b; Table 3 of ESM). Compared to the actinolite cores of the amphibole crystals in the matrix, the S_2 inclusions are less magnesian and aluminous, and more calcic (Fig. 4; Tables 2, 3 of ESM).

Optical zoning in garnet porphyroblasts correlates with chemical zoning (Fig. 3 of ESM). Garnet core ($g1_C$) is characterised by an increase in almandine (Alm43 → 49 %) and a decrease in grossular (Grs35 → 31 %) and spessartine (Sps20 → 16 %). X_{Fe} remains constant (X_{Fe} = 0.94–0.95) and the proportion of pyrope varies irregularly between 2 and 3 % (Fig. 3a-profile 1 of ESM; Table 3 of ESM). According to the different behaviour of grossular and spessartine, it is possible to distinguish two areas. The intermediate area ($g1_R$) is characterised by an increase in the amount of both almandine and grossular, and a strong decrease of the proportion of spessartine (Alm48 → 56 %, Grs31 → 37 %, Sps18 → 5 %), whereas X_{Fe} and the proportion of pyrope show only small variations with respect to the core values (Fig. 3a-profile 1 of ESM; Table 3 of ESM). In the external area ($g2_C$), the rimward evolution is characterised by a decrease in grossular, spessartine and X_{Fe} (Grs37 → 28 %, Sps5 → 2 %, X_{Fe} = 0.95 → 0.89 %), accompanied by an increase in almandine and pyrope (Alm56 → 61 %, Prp3 → 9 %) (Fig. 3a-profiles 1 and 2 of ESM; Table 3 of ESM). Finally, in the outermost rim ($g2_R$): almandine and X_{Fe} first decrease before increasing again (Alm61 → 59 → 61 %, X_{Fe} = 0.89 → 0.84 → 0.86 %), pyrope first increases (Prp9 → 12) and then locally decreases (Prp12 → 10) grossular and spessartine decrease (Grs30 → 27 %, Sps2 → 1 %; Fig. 3a-profile 1 of ESM; Table 3 of ESM).

Garnet grains included in the pseudomorphs are in general smaller (0.25–0.65 mm) and are chemically equivalent to the inner part of garnet 2 ($g2_C$; Fig. 3b-profile 3 of ESM; Table 4 of ESM). Smaller garnet grains scattered in the matrix (0.5–1.5 mm; Fig. 3a-profile 2 of ESM; Table 3 of ESM) and the ones included in the albite porphyroblasts (<0.5 mm; sample AG) are chemically equivalent to the outer part of garnet 2 ($g2_R$).

Pseudomorphs after lawsonite

The lawsonite pseudomorphs are distinctly white in hand specimen and up to 2 cm long. The original porphyroblasts are completely replaced by aggregates showing, in the less deformed areas, the typical rectangle or rhombus shape of fresh lawsonite (Fig. 5a). Minerals forming the aggregates are typically dominated by fine-grained prisms of zoned epidote (type 2b) with small titanite inclusions (type 2b; <5 μm), rutile partially replaced by ilmenite (type 2), chlorite (type 2) and albite (type 2). Almandine-rich garnet ($g2_C$; <0.65 mm) is randomly scattered in the pseudomorphs and contains very fine-grained inclusions (<0.01 mm) of epidote, titanite and quartz (Fig. 3b of ESM). Additionally, white mica and amphibole, if present, are exclusively concentrated in specific areas of the pseudomorphs (Fig. 2b; Table 4 of ESM). White micas are individual crystals of phengitic muscovite (type 2; up to 3.5 Si pfu) or fine-grained intergrowths of muscovite and paragonite (<2 μm; below electron microprobe resolution; Fig. 2g of ESM). Paragonite is not present in the matrix foliation, and phengitic muscovite in the pseudomorphs shows slightly higher Si contents than the ones in the matrix foliation. Amphiboles are acicular (10–15 μm) to prismatic (<70–100 μm) unzoned crystals of actinolite (type 2b) chemically equivalent to the crystals included in g2 (Table 3 of ESM), and barroisitic hornblende (type 2), which is poorer in Si and Mg and richer in Na and Ti than the crystals in the matrix foliation and in the pressure tails (Table 4 of ESM). Inclusions of glaucophane have been described in the pseudomorphs by Rodríguez Aller (2005), but have not been identified in this study. Actinolite crystals are chemically equivalent to the crystals included in garnet 2. Barroisitic hornblende from the pseudomorphs is

chemically different to the crystals of the matrix foliation and the pressure tails, being poorer in Si and Mg and richer in Na and Ti (Table 3 of ESM).

As exposed above, within the aggregates forming the pseudomorphs, it is possible to distinguish two individual sets of stretched clusters defining an internal curved foliation. The first group is composed by albite, chlorite and, frequently, epidote crystals. The second type of clusters is composed of rutile, ±ilmenite and titanite. Titanite occurs as partial or complete coronas around rutile, locally replaced by ilmenite in the outermost rims (Fig. 2h of ESM). This curved pattern is oblique to the matrix foliation inside the pseudomorph and continuous with it in their outer zones. In general, epidote prisms show an oblique orientation with respect to the pseudomorph rims. Clusters orientation is more evident as deformation increases. Finally, the outermost areas of the pseudomorphs overgrow an amphibole–epidote–titanite foliation (S_2). These features suggest that lawsonite crystals were synkinematic with the matrix foliation. Towards the top of the lithological sequence, the lawsonite pseudomorphs become more deformed (Fig. 5e). Locally, the matrix of the albite-bearing rocks contains stretched and folded aggregates of epidote, white micas and albite that can be interpreted as strongly deformed lawsonite pseudomorphs by comparison to the neighbouring rocks. Hence, it can be inferred that with increasing strain intensity, lawsonite pseudomorphs were strongly deformed and became progressively incorporated into the matrix.

Sample AG

To the top of the succession, as exemplified by sample AG, the main foliation is defined by the shape-preferred orientation of Ca amphibole, epidote (type 3), chlorite (type 3a), phengitic muscovite (type 3; with Si < 3.4 pfu), and minor amounts of titanite (type 3), ilmenite (type 3) and quartz (Fig. 5c; Table 5 of ESM). Amphiboles are unzoned actinolite (type 3) and hornblende (type 3). This foliation

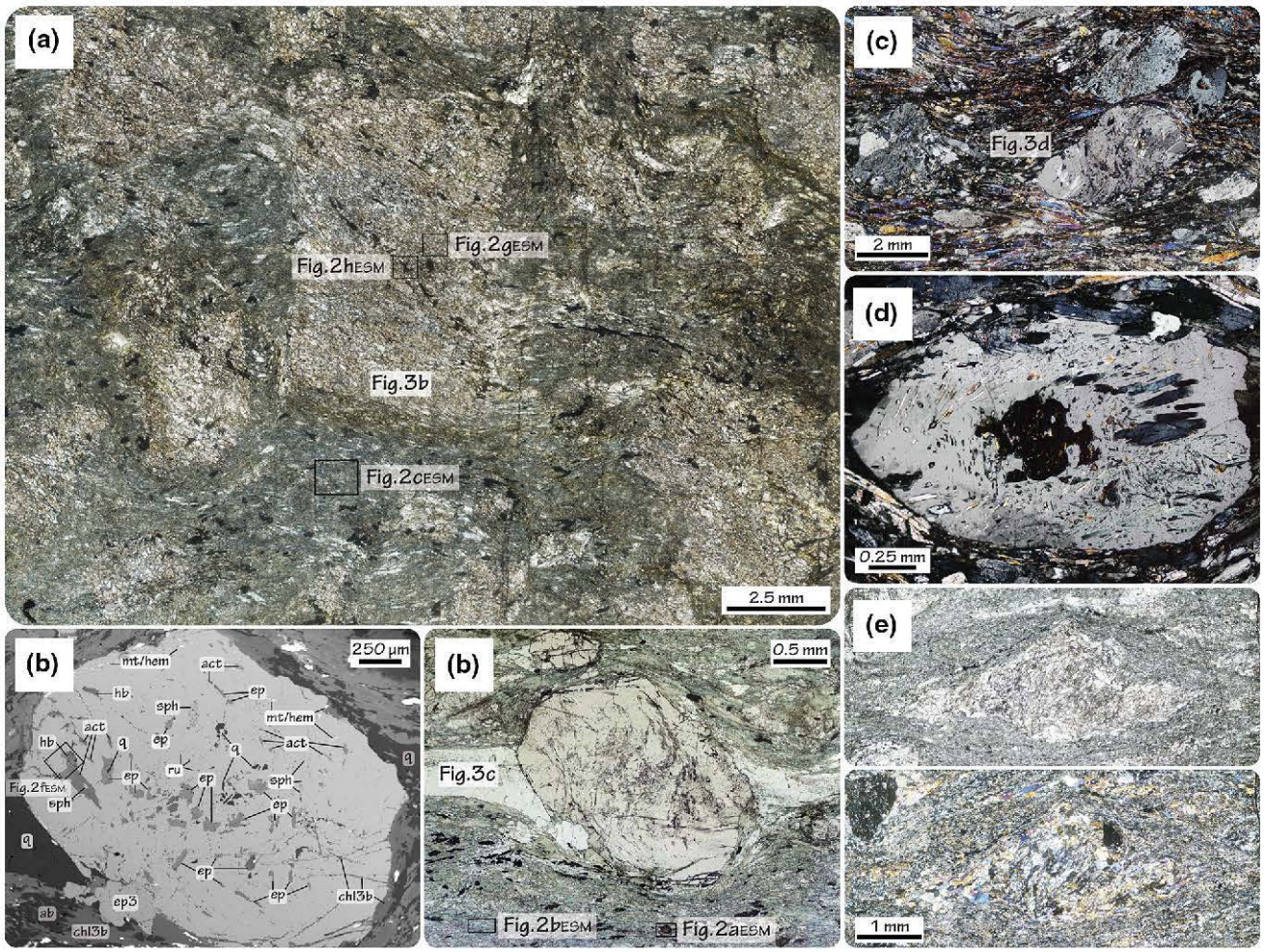

Fig. 5 Microphotographs of thin-section images of the Cambre metabasic rocks showing **a** euhedral lawsonite pseudomorphs (sample CA); **b** garnet porphyroblasts displaying curved inclusions; **c** albite-bearing samples (sample AG); **d** strongly stretched pseudomorphs after lawsonite almost indistinguishable from the matrix foliation

wraps around coarse-grained subhedral to anhedral porphyroblasts of albite (type 3; up to 3 mm long). Albite porphyroblasts are only present in the uppermost levels of the sequence and do not coexist with euhedral lawsonite pseudomorphs. Porphyroblasts contain linear, curved, folded or helicitic inclusion trails well defined by minerals of variable size (5–200 μm) and continuous with the S_3 foliation (Figs. 2c, 5c). Inclusion trails comprise the same phases as the matrix foliation. Amphiboles in the S_3 foliation are slightly richer in Ca and poorer in Al and Na than S_2 amphiboles (Fig. 4). Albite also locally contains inclusions of anhedral grains of garnet ($g2_R$; Fig. 5d) and apatite.

Finally, post-S_3 phases include magnetite, haematite and sulphides concentrated along localised shear planes and carbonates locally overgrowing the S_3 foliation. Other late features include the occurrence of chlorite in fractures and the partial to complete replacement of garnet by chlorite flakes (type 3b; Table 5 of ESM).

Three stages of blastesis are distinguished in the evolution of the Cambre metabasic rocks (M_1, M_2 and M_3). The M_1 episode is preserved as a relict S_1 assemblage that comprises inclusions of ep-sph-ru-q within the first generation of garnet (g1). It is followed by a second metamorphic stage, M_2, characterised by the syntectonic development of an assemblage including lawsonite, a second generation of garnet (g2) and a foliation (S_2) consisting of law*-ep-act/bar ± gl*$^{\#}$-o*$^{\#}$-mu-ru/ilm-sph-q (see symbols in electronic supplementary material). This assemblage is preserved at the base of the upper sequence of the MTC. The third stage M_3 is best developed at the top of the sequence. It is characterised by the growth of syntectonic albite porphyroblasts and a foliation S_3 containing ep-act-hb-mu-chl ± ilm-sph-q. Whereas both, S_2 and S_3, have the same orientation, first-order petrographic observations suggest that they developed at distinct *P–T* conditions. Finally, post-M_3 crystallisation includes post-S_3 phases such as mt, hem, chl, carb, sul and q, variably present in most samples of the Cambre metabasic rocks.

P–T–X evolution: pseudosection modelling

In order to constrain the *P–T* path for the Cambre metabasic rocks, the observed mineral assemblages and chemical compositions have been compared with the stability and compositions of phases in *P–T–X* pseudosections. Pseudosections were calculated using THERMOCALC 3.33 and 3.37 (Powell and Holland 1988) and the internally consistent thermodynamic dataset (Holland and Powell 1998; updated Nov. 2003). References of the mixing models for solid solutions of the phases considered in the calculations are: amphibole and clinopyroxene (Diener and Powell 2012), garnet (White et al. 2007 modified by Diener et al. 2008), chlorite (Holland et al. 1998), white mica (Smye et al. 2010), plagioclase (Holland and Powell 2003), epidote (Holland and Powell 1998), magnetite (White et al. 2000), ilmenite and hematite (White et al. 2000). Bulk-rock composition was obtained by X-ray fluorescence on a crushed rock slab of sample CA. FeO (vs. Fe_2O_3) was analysed by wet chemical titration. The fluid phase was fixed as pure H_2O, initially in excess. Phase relations were modelled in the chemical system Na_2O–CaO–K_2O–FeO–MgO–Al_2O_3–SiO_2–H_2O–TiO_2–Fe_2O_3 (NCKFMASHTO) between P = 0.5–2.6 GPa and T = 350–600 °C. The original composition of the studied rocks was simplified to fit this system (Table 1). Because activity–composition relations for Mn-bearing solid solutions are poorly constrained and the studied sample has a low MnO content (0.22 wt%; Table 1), which is exclusively concentrated in the garnet cores, MnO was not included in the chemical model system. The diagrams are shown in Fig. 6, where white fields are divariant and increasing variance is shown with progressively darker shades. Mineral abbreviations are those used by THERMOCALC (see electronic supplementary material).

As a first approach, a H_2O-saturated *P–T* pseudosection was computed for the analysed bulk-rock composition (Fig. 6a). In the diagram, quartz is stable across the entire *P–T* range and TiO_2 is chiefly contained in rutile at $P > 1.5$ GPa and in titanite for $P < 1.5$ GPa. Glaucophane is stable in most of the fields, with the exception of low pressures and high temperatures where hornblende is stable. Glaucophane commonly occurs with actinolite and omphacite in the H*P*–L*T* part of the diagram. Muscovite is stable at $P > 6$–15 kbar, depending on the temperature, whereas biotite is stable at low pressures. The equilibration conditions of the relic M_1 assemblages included in the Mn-rich garnet core cannot be quantified in this diagram because MnO has not been considered in the calculations (see above) and it extends significantly the stability of garnet towards lower *P* and *T* (e.g. Tinkham et al. 2003; Zuluaga et al. 2005).

Nevertheless, garnet zoning can be used qualitatively to constrain the *P–T* evolution associated with the crystallisation of the garnet core (g1). The preserved zoning, in particular the decrease in the proportion of spessartine, suggests that the first generation of garnet (g1) grew along the prograde *P–T* path in an epidote-bearing rock (as ep is an inclusion in g1). By comparison with the interbedded pelitic rocks, M_1 can be roughly constrained at ≈1.2–1.4 GPa, 350–380 °C (López-Carmona et al. 2013).

The coexistence of lawsonite, epidote and garnet in the syn-S_2 assemblage (law*-ep-act/bar ± gl*$^{\#}$-o*$^{\#}$-mu-ru/ilm-sph-q) gives strong *P–T* constraints in the framework of the present pseudosection. The three minerals are stable together only in a relatively narrow domain at $T > 550$ °C and $P > 2$ GPa. The calculated amount of the phengitic substiution in muscovite in this domain (Si = 3.36–3.46 pfu;

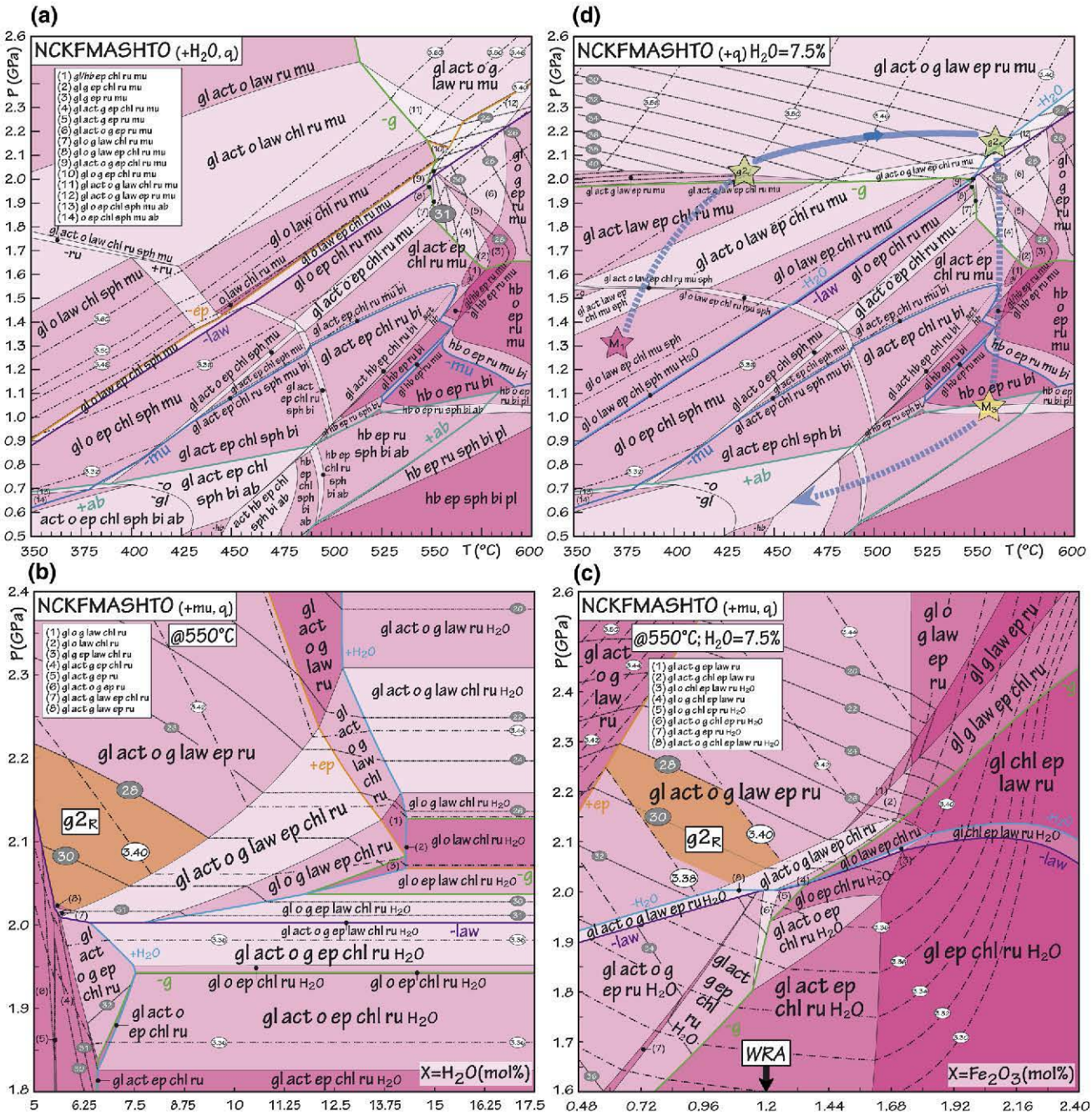

Fig. 6 Sample CA [SiO_2:53.28; TiO_2:1.60; Al_2O_3:8.76; FeO:7.90; Fe_2O_3:1.76; MgO:11.79; CaO:11.72; Na_2O:3.15; K_2O:0.05] **a** *P–T* pseudosection with H_2O in excess; **b** *P–X*(H_2O) pseudosection calculated at 550 °C for the analysed bulk-rock composition showing H_2O-out line; **c** *P–X*(Fe_2O_3) pseudosection calculated at @550 °C for H_2O = 7.5 mol.%; WRA—original whole-rock analysis from XRF; **d** *P–T* pseudosection with H_2O = 7.5 mol.%. Note that the H_2O ratio (7.5 mol.%) was obtained graphically. Recalculated proportions are shown in Table 1

Fig. 6a) fits well that is observed in the S_2 foliation (Si = 3.38–3.46 pfu). However, the measured proportion of grossular in garnet decreases in g2 from 38 to 28 mol.%, whereas the maximum grossular value modelled in the pseudosection only reaches 31 %, and this value is only compatible with the composition of the rim of g2. Nevertheless, this pseudosection provides a suitable starting point for assessing the effects of the components H_2O and Fe_2O_3 that are difficult to quantify reliably using chemical analyses of rocks, but that usually have significant influence on phase equilibria, and hence on the *P–T* estimates. Furthermore, the metamorphic study of the interbedded pelitic

rocks revealed that (1) their prograde evolution occurred in fluid undersaturated conditions due to the crystallisation of lawsonite and (2) the bulk Fe_2O_3 in the metapelites did not reflect the oxidation state during the main metamorphic evolution (López-Carmona et al. 2013). Given these results, a particular attention on these aspects is necessary for the modelling of CA.

The available amount of H_2O has an influence on the position of the compositional isopleths. Estimating the amount of H_2O available in the system at peak conditions may help to reduce the uncertainty concerning grossular isopleths. For this, a P–$X(H_2O)$ pseudosection was calculated at 550 °C (Fig. 6b). The temperature corresponds to that predicted at H_2O saturation conditions for the coexistence of epidote, lawsonite and garnet at the maximum content of grossular predicted in the pseudosection (Fig. 6a). However, other temperature values have been tested and the exact value does not have a significant effect on the result. In the new diagram, the assemblage that would have been stable during the crystallisation of g2 is stable above 2 GPa at H_2O-undersaturated conditions in the field gl-act-o-g-law-ep-ru-mu-q. In this area the, Si content in S_2-muscovite (typically between 3.38–3.42 pfu) and the X_{Ca} isopleths for the rim composition of g2 (Grs31–28 %) intersect between 2 and 2.1 GPa and 5–10 % H_2O (shaded area in Fig. 6b). Therefore, for the subsequent calculations, the amount of H_2O was fixed at a mean value of 7.5 mol.% (obtained graphically; See normalized compositions in Table 1). The H_2O-out line and the law-out line are almost coincident within this interval, suggesting that the rock reached H_2O-undersaturation due to the crystallisation of lawsonite.

With the estimated amount of H_2O (7.5 mol.%) a P–$X(Fe_2O_3)$ pseudosection at 550 °C was calculated to evaluate the effects of varying the Fe_2O_3 content ("O" in the bulk composition; Fig. 6c). Other temperatures have been tested and the exact value does not have a significant effect on the result. Following the above-mentioned procedure, in the diagram, the assemblage in equilibrium with g2 (gl-act-o-g-law-ep-ru-mu-q) is stable in the H_2O-undersaturated region in a large area above 1.9 GPa, where the relevant isopleths for the rim composition of g2 and the Si content in phengitic muscovite (Grs = 31 → 28 %; Si(mu) = 3.38–3.42 pfu) intersect between 1.9 and 2.2 GPa and 0.6–1.2 % Fe_2O_3 (shaded area in Fig. 6c). Therefore, this diagram yields no tight constraints on the amount of Fe_2O_3 present in the rock, although it excludes values significantly higher than the analysed one.

Based on the inferred estimations, with the aim of establishing the P–T evolution for the CA at peak conditions, a new P–T pseudosection fixing the amount of H_2O = 7.5 mol.% was recalculated in the NCKFMASHTO system (Fig. 6d). Compared to the original diagram (Fig. 6a), in this P–T pseudosection, the stability of garnet increases significantly in the H_2O-undersaturated region towards lower P (down to 2 GPa) and T, and epidote is stable in all the diagram. Thus, the stability of assemblages containing g + law + ep extends towards low temperature and high pressures. The paragenesis corresponding to the M_2 stage is located at pressures higher than 2 GPa, in the trivariant fluid-absent field gl-act-o-g-law-ep-ru-mu-q, and the fluid-present equivalent field (label 12 in Fig. 6d). Based on textural observations, this stage of the metamorphic evolution involves crystallisation of both lawsonite and garnet 2. In the diagram, the X_{Ca} isopleths for the core of garnet 2 and those calculated for the Si content in S_2-muscovite (Grs = 37 %; Si (mu) up to 3.5 pfu) intersect between 2–2.1 GPa at 430–440 °C (shaded star, $g2_C$, in Fig. 6d). The continuous decrease in grossular (37 → 28 %) suggests that garnet 2 rims equilibrated at 2.2 GPa and 550–565 °C. Further evolution involved decreasing pressure, leading to the destabilisation of lawsonite and crossing the solvus between Na and Ca amphiboles. Above the solvus, at higher P, the mode of glaucophane is systematically higher than the mode of actinolite. Close to the solvus, z in glaucophane decreases and c increases, and the opposite occurs in actinolite. Thus, glaucophane becomes less sodic and more calcic, and vice versa for actinolite. On decompression, below the solvus, the amount of Al^{VI} (y) in glaucophane decreases progressively as it approaches the domain where the three amphiboles (gl, act and hb) coexist. In this region, both glaucophane and hornblende have a similar y, which suggests that glaucophane can progressively recrystallise with compositions approaching those of hornblende. This is compatible with the observed rimward decrease of Al in the analysed amphibole crystals (Table 2 of ESM). Beyond the solvus, actinolite disappears and the mode of hornblende is systematically higher than the mode of glaucophane, which does not exceed 10 % (whereas the mode of hornblende is 50 %). From this point, the exhumation can be followed in the gl-out domain. The M_3 stage is defined by the appearance of albite at $P < 1.1$ GP, suggesting a decompression from the law-bearing fields to the fields with stable albite at $P \approx 1$–1.1 GPa and $T \approx 550$–560 °C and a further cooling to the glaucophane and omphacite-absent field act-hb-ep-chl-bi-sph-ab-mu-q at $P \approx 0.6$–0.7 GPa and $T \approx 440$–480 °C.

$^{40}Ar/^{39}Ar$ geochronology

Timing constraints on the P–T evolution of HP terranes are essential in understanding the subduction–exhumation process. Whilst the ages of various events of the lower allochthon of the MTC have been extensively studied, the data for the middle allochthon are limited to only one $^{40}Ar/^{39}Ar$ age on muscovite of 348 ± 8 Ma (Rodríguez

Aller et al. 2003). Therefore, one of the objectives of this study was to date white mica and amphibole separates from blueschist facies fabric and the mylonites of the basal contact by $^{40}Ar/^{39}Ar$. For this purpose, three samples were selected: one mylonite developed in the felsic gneisses just below the Cambre metabasic rocks (sample MT1), a pelitic schist interbeded with the Cambre metabasic rocks (sample LM, for lower metapelites, from Lo´pez-Carmona et al. 2013) and one sample of the Cambre metabasic rocks with euhedral lawsonite pseudomorphs (sample CA). The loca-tion of the dated samples and their relative structural position are shown on Fig. 1c and Fig. 2 of ESM.

Sample selection

The main goal of dating the mylonites (sample MT1) separating the lower and the middle allochthon in the MTC (Bembibre–Ceán detachment; Fig. 1a, c) is to establish the age of the early regional extensional phases that led to the orogenic collapse in the allochthonous complexes of NW Iberia (e.g. Martínez Catalán et al. 2002; Gómez Barreiro et al. 2010; Díez Fernández et al. 2012). Sample MT1 is a fine- to medium-grained (0.1–1 mm) mylonite developed in the granitic orthogneisses of the MTU. It consists of millimetre-scale alternations of chlorite and muscovite and disrupted quartz ribbons that define a banding preserved between extensional shear bands. The phylosilicate domains contain white mica porphyroclasts (0.1–1 mm) with strong undulate extinction and kink-bands, K-feldspar phenocrysts showing partial to complete saussuritisation/sericitisation (0.4–0.8 mm), epidote (up to 0.5 mm long) crystals and suhedral to anhedral garnet grains (<0.3 mm). The deformation gradient related to this contact decreases both upward and downward, with secondary ultramylonitic shear zones occurring several metres above and below the main shear zone (Fig. 1c; Díez Fernández et al. 2012).

Sample LM was chosen based on its textural equilibrium, characterised by a well-preserved peak mineral assemblage (S_2) mainly preserved as relict micro-inclusions in the rim of garnet porphyroblasts and in specific domains of the matrix foliation. Sample LM shows a medium-grained (0.2–4 mm) porphyro-lepidoblastic texture and a well-developed planar to plano-linear fabric. White mica and quartz constitute >50 %, and locally up to 80 %, of the modal proportion of each sample. The foliation is defined by the shape-preferred orientation of phengitic muscovite, paragonite and chlorite. In these pelitic schists, the matrix foliation usually obliterates an early fabric resulting in a composite foliation $S_2 + S_3$. Whereas S_2 is interpreted as the foliation preserved from the subduction-related blueschist facies prograde metamorphism, S_3 correspond to the early-exhumation event (López-Carmona et al. 2013). Finally, the interbedded Cambre metabasic rocks are usually more retrogressed, and the H*P* fabric is commonly overprinted by the amphibolite–greenschist facies fabrics.

$^{40}Ar/^{39}Ar$ stepwise heating results

$^{40}Ar/^{39}Ar$ step heating analyses on single grains and concentrates of muscovite and hornblende were performed on each of the selected samples. In this paper, it is considered that a reliable plateau age is obtained when the apparent ages of at least three consecutive steps, comprising a minimum of 50 % of the $^{39}Ar_k$ released (cf. Fleck et al. 1977), agree within 2σ error with the integrated age of the plateau segment. The age spectra are shown in Fig. 7 and the corresponding data on Tables 7, 8, 9 and 10 of ESM, where ages are reported at $\pm 2\sigma$ (95 % confidence level).

The apparent age spectrum from sample MT1 muscovite (Fig. 7a) shows very young apparent ages in the low-temperature steps that rapidly increase to a plateau age of 337 ± 3 Ma (Steps 8–13, MSWD = 1.84) defining 56 % of the ^{39}Ar released. Because the low- and high-temperature steps in the age spectrum appear to be associated with both elevated Ca/K and Cl/K ratios (Table 7 of ESM), the apparent ages from these steps are interpreted to reflect possible very minor contamination from minute inclusions in the mica crystal. The integrated age of the sample is 325 ± 3 Ma. A replicate sample also yields similar plateau and integrated ages (337.3 ± 2.84 and 326.16 ± 2.50 Ma, respectively).

Two $^{40}Ar/^{39}Ar$ step heating analyses on muscovite concentrates from sample LM give two identical plateau ages of 354 ± 1 Ma (71 % of the ^{39}Ar released, MSWD = 1.31; and 67 % of the ^{39}Ar released, MSWD = 1.23, respectively) (Fig. 7b, c). A single-grain analysis of a phengite crystal (~1,500 μm) yielded an older age of 363 ± 2 Ma (98.5 % of the ^{39}Ar released, MSWD = 0.72) (Fig. 7d).

In sample CA, the step heating analyses of a concentrate of hornblende unfortunately yielded no reliable results. Several analyses of hornblende provided integrated ages ranging from 620 to 800 Ma, which are significantly older than the age of metamorphism (and are therefore not shown because they are geologically meaningless). These amphiboles are strongly zoned, suggesting that either the amphibole integrated ages reflect inherted Ar from older amphibole cores (e.g. Villa et al. 2000) or some minor excess argon was present in the rock.

Ar retention record and closure temperature

Diffusive-like behaviour of Ar in micas is one of the main advantages in linking $^{40}Ar/^{39}Ar$ dates to *P–T* histories. Dodson (1973) formulation of closure temperature has

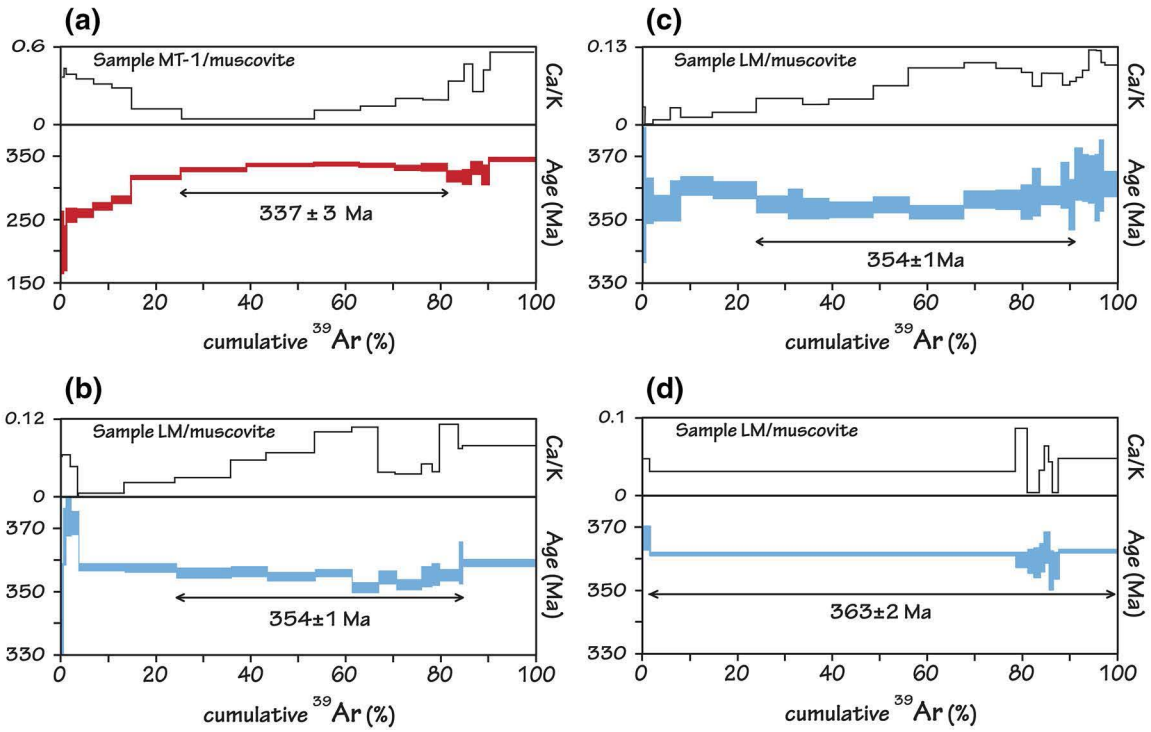

Fig. 7 $^{40}Ar/^{39}Ar$ step heating results from samples MT1 (**a**) and LM (**b–d**)

been often used to estimate the mean closure temperature in cooling geochronological systems. However, recent studies (e.g. Harrison et al. 2009) suggest that there may be a significant pressure dependence of Ar diffusion in muscovite, such that Dodson's closure-temperature model may not be applicable in all metamorphic scenarios, and especially to those that have experienced relatively rapid orogenic cycles (e.g. Warren et al. 2008a, b, 2012). Therefore, linking an apparent muscovite $^{40}Ar/^{39}Ar$ age to a single closure temperature must be done cautiously (e.g. Warren et al. 2012). The closure temperature of muscovite (and broadly, white mica) in the K–Ar isotopic system has been extensively discussed [e.g. Rodrı´guez Aller et al. (2003), Bosse et al. (2005) and Pitra et al. (2010)] in similar rocks of Variscan age. Currently, several studies using $^{40}Ar/^{39}Ar$ dating in H*P* terranes show that the iso-topic closure temperature for white micas in the blueschist facies conditions may be ~500 °C for muscovite (Villa et al. 2000; Bosse et al. 2005; Harrison et al. 2009) o r >550 ° C for phengitic muscovite (Lister and Baldwin 1996; Pitra et al. 2010).

In the present study, we interpret the significance of the metamorphic muscovite $^{40}Ar/^{39}Ar$ ages using the time-integrated finite-difference program of Lee (1995) t o numerically model Ar diffusion in the muscovites during the exhumation of the middle allochthon. Through the selection of appropriate model parameters, solid-state Ar diffusion can be modelled in an identical fashion to the numerical models of Wheeler (1996) and Lister and Baldwin (1996). We use exhumation rates consistent with a cooling rate of 20 °C/Ma [typical of H*P*–L*T* terranes, e.g. Ernst (1973) and Newton and Fyfe (1976)], peak P–T conditions estimated for sample LM (≈2.1 GPa and ≈460 ° C; Lo´pez-Carmona et al. 2013), the Ar diffusion parameters in muscovite from Harrison et al. (2009) and muscovite grain radii between 0.1 and 1 mm.

Understanding the significance of the Ar ages is important because of the potential for excess Ar in blue-schist facies regimes which can be incorporated into the minerals during crystallisation and exhumation (e.g. Warren et al. 2010; Sherlock et al. 1999; Ruffet et al. 1995). Thus, we examine two scenarios of open-system Ar-diffusive behaviour: (1) where it is assumed that there is a zero boundary concentration of Ar during exhumation and (2) where it is assumed there is some excess Ar at the grain boundary. Assuming a zero boundary concentration of Ar during exhumation, the numerical modelling indicates that the peak metamorphic temperature is low enough and the exhumation is so fast that almost no Ar is lost from the samples during crystallisation. Assuming the presence of excess argon, the numerical modelling shows that the mean diffusion distance is less than the grain radius of all of the muscovite grains, indicating that there should be a distinct age gradient from the rim to the core of the grains under the given *T*–*t* conditions. As the resultant muscovite age spectra in Fig. 7 do not reveal the presence of an inward

age gradient consistent with the inward diffusion of excess Ar, the modelling results strongly support the conclusion that there has not been significant uptake of excess Ar (even if present in the rock), and the muscovite plateau ages are best interpreted as crystallisation ages.

Discussion

Phase diagrams: consistency between calculations and natural assemblages

Calculated phase diagrams account reasonably well for the first-order petrographic observations. Pseudosection calculations indicate that the prograde evolution would have occurred in H_2O-undersaturated conditions induced by the crystallisation of lawsonite, as demonstrated for the interbedded metapelitic rocks by Lo´pez-Carmona et al. (2013). The transition from lawsonite blueschist/*LT*-eclogite to amphibolite–greenschist facies may involve significant hydration (e.g. Schliestedt and Matthews 1987; Barrientos and Selverstone 1993; Bosse et al. 2002), principally as a result of lawsonite breakdown (cf. Balle`vre et al. 2003; Clarke et al. 2006; L´o pez-Carmona et al. 2013). Thus, the H_2O content appears to be a critical factor in the metamorphic evolution of the Cambre metabasic rocks. Nevertheless, the modelling failed to reproduce some of the petrographic observations. First, the stability of titanite in the pseudosections, limited to low pressures, whereas it is a common phase in all assemblages, as inclusions and in the matrix. This may be explained by the fact that titanite is considered as a pure end-member in the model, whereas analysed titanite has small, but non negligible, substitutions of Al and Fe (ranging from 1 to 2 wt% and up to 1.2 wt%, respectively; Tables 2, 3, 4 and 5 of ESM). This is rather common, particularly at high pressures (e.g. Franz and Spear 1985; Hole´nyi and Annerstein 1987; Enami et al. 1993; Tropper et al. 2002; Harlov et al. 2006; Manon 2008). Al-thought minor, these substitutions (that commonly do not exceed a couple of weight%) could significantly extend the stability of titanite and explain this apparent incompatibility between the observations and the predictions in the calcu-lated phase diagrams. Second, the model does not predict ilmenite and paragonite. In a hydrated MORB system ilmenite is expected to stabilise at L*P*–H*T* conditions (Liou et al. 1998; Meinhold 2010), whereas rutile or titanite are the dominant Ti-bearing minerals in the *P*–*T* range of the pre-sented phase diagrams. Ilmenite occurs, replacing rutile, and is associated with titanite coronae as a late phase during the retrograde metamorphism. Its crystallisation thus probably reflects local equilibrium and cannot be reliably modelled in a phase diagram that supposes equilibration at the scale of the entire sample. Although the coexistence of these three Ti–rich phases is well known, it has not yet been constrained experimentally (Liou et al. 1998). Additionally, the modelled chemical system is Mn-free, and ilmenite contains up to a 2 wt% of MnO, which can extend its stability domain.

Similarly, paragonite is exclusively present as a product of destabilisation of lawsonite (it is not present in the matrix foliation). This process cannot be accounted for appropriately in the framework of diagrams calculated for the analysed bulk composition of the sample. Indeed, the pseudomorphic replacement of lawsonite by the epi-dote + phengite/paragonite + chlorite + albite ± quartz aggregates reflects equilibration in volumes close to the size of the lawsonite crystals, and hence an effective bulk composition (e.g. Tracy 1982; Stu¨we 1997) significantly different from that of the entire sample. Finally, biotite is modelled at $P <$ 1.4 GPa, but not observed in the Cambre metabasic rocks. However, the proportion of biotite pre-dicted in the diagram reaches a maximum of 0.7 % along the proposed *P*–*T* path and further decreases with decreasing temperatures. Therefore, biotite could have been stable but not observed, for example, because it was chloritised during retrogression.

Lawsonite crystallisation in the blueschists

Lawsonite crystals in the Cambre metabasic rocks are entirely pseudomorphed by an aggregate of epi-dote + phengite/paragonite + chlorite + albite ± quartz. The breakdown products of lawsonite may follow a reac-tion g + gl + law = chl + ep + mu/pa + H_2O (cf. Will et al. 1998; Balle`vre et al. 2003) and may represent the onset of retrogression into the amphibolite–greenschist facies (e.g. Shelley and Bossie`re 1999). Modelling suggests that the S_2 foliation was glaucophane-bearing. Due to the retrograde overprint during the transition from the blue-schist/*LT*-eclogites to the amphibolite–greenschist facies conditions, almost all traces of the destabilisation of former phases were destroyed. However, relict textures as the re-crystallised symplectitic intergrowth of hornblende and albite in the matrix foliation, and the chlorite–albite aggregates inside the pseudomorphs, may represent the replacement of former crystals of glaucophane. Moreover, in the interbedded pelitic rocks, glaucophane was found in the S_2 foliation preserved as relict microinclusions in the rim of garnet porphyroblasts, confirming its occurrence during M_2 in the Cea´n Unit.

Despite complete retrogression, the preservation of some of the lawsonite crystal shapes indicates that pseudomorphism occurred as a static process (e.g. Balle`vre et al. 2003) and particular levels of the blueschist host rock were not affected by penetrative deformation during exhumation (e.g. Philippon et al. 2013). Petrographic observations and phase diagram calculations suggest that the second

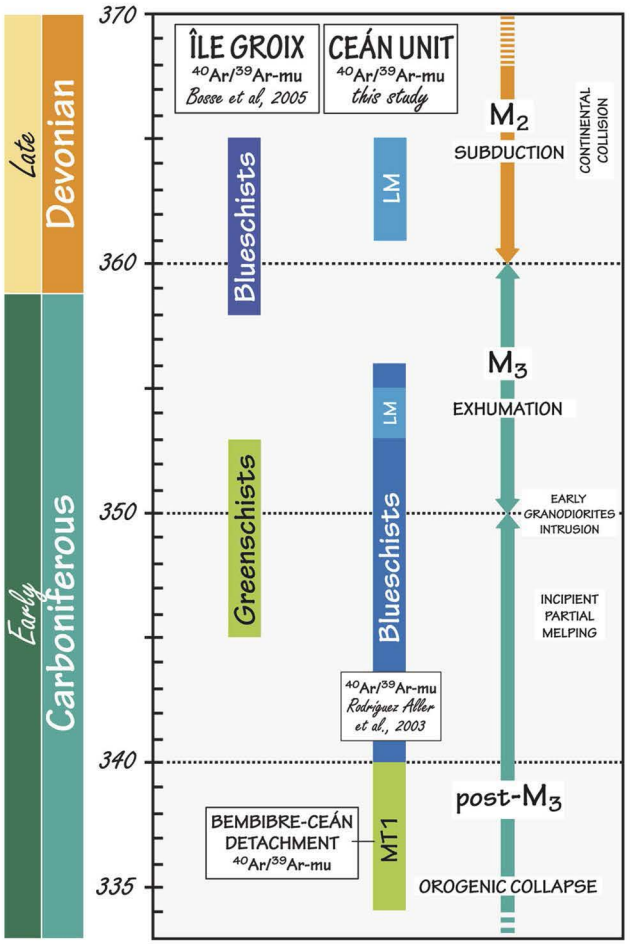

Fig. 8 Synthesis of the $^{40}Ar/^{39}Ar$ ages from the blueschists in the middle allochthon of the Ibero-Armorican Arc. The interpretation on the age of the metamorphic stages is also indicated. Devonian-Carboniferous boundary after Walker et al. (2012)

generation of garnet grains (g2) and lawsonite crystallised at peak conditions in the matrix assemblage (M_2), and replacement took place at decreasing pressure, in the early almost isothermal decompression stages (post-M_2) (Fig. 6d).

Metamorphic evolution of the Ceán Unit

The *P–T* evolution of the Cea´n Unit comprises three metamorphic episodes (M_1–M_3; Fig. 9). The first episode (M_1) represents the early subduction-related stages and is only preserved in the lower structural levels of the sequence. The second metamorphic stage, M_2, characterises the subduction-related blueschist facies prograde metamorphism. It is evidenced by the syntectonic development of lawsonite–glaucophane-bearing assemblage preserved at the base and in the middle part of the sequence. Finally, the exhumation-related metamorphism (M_3) is best developed at the top of the sequence and defined by the growth of syntectonic albite porphyroblasts during the nearly isothermal decompression.

Differences in the temperatures recorded by the metapelitic and the metabasic rocks comprising the Cea´n Unit (Fig. 9) are interpreted as a result (or a combination) of (1) their different position in the orogenic wedge within the subduction complex (cf. Lo´pez-Carmona et al. 2013; Fig. 10), (2) the thermal effects of fluid migration during metamorphism (e.g. Peacock 1987; Stober and Bucher 2004; Dipple and Ferry 1992; Wing and Ferry 2002; Lyubetskaya and Ague 2009) or (3) related to shear heating effects that may have favoured a temperature increase with deformation. The conversion of mechanical energy into heat is a well-know processes (e.g. Duprat-Oualid et al. 2013; Gottardi et al. 2013; Souche et al. 2013). The deformation gradient related to the contact between the lower and the middle allochthons decreases both upward and downward. Accordingly, the two samples with the highest equilibration temperature (CA and UM) are located immediately above a shear zone. Sample CA, showing the highest temperature (560 °C), is located just above the main shear zone, and sample UM is located just above a secondary mylonitic band (Fig. 1c). Thus, temperature seems to increase with deformation.

However, it should also be stressed out that the absolute accuracy of the *P–T* estimation based on pseudosections should not be overestimated. The main advantage of this approach is the determination of the qualitative evolution of the rocks. The absolute values are subject to a certain degree of uncertainty, related among others to the accurate estimation of the effective bulk-rock composition (and its possible evolution along the *P–T* path) and the accuracy of the mixing models for solid solutions. It is therefore possible that the difference in the absolute *P–T* conditions recorded by the metapelitic and metabasic samples may be within an acceptable error.

Age of the metamorphism in the MTC

$^{40}Ar/^{39}Ar$ step heating of phengitic muscovite from the pelitic schists yield plateau ages of ca. 363 ± 2 and 354 ± 1 Ma. The older age obtained in this study is interpreted as the minimum age of the M_2 blueschist facies metamorphism in the middle allochthon of the MTC. This age is a minimum because M_1, recorded by both metapelites and metabasic rocks, remains unconstrained. M_1 is recorded by aligned inclusions in the core of garnet porphyroblasts, and in situ laser ablation analyses were not performed. The age of ca. 365 Ma is consistent with the other muscovite plateau ages of ca. 355 Ma, which are inferred to represent some point relatively close to peak conditions at the onset of the isothermal decompression. These ages are in agreement with the available

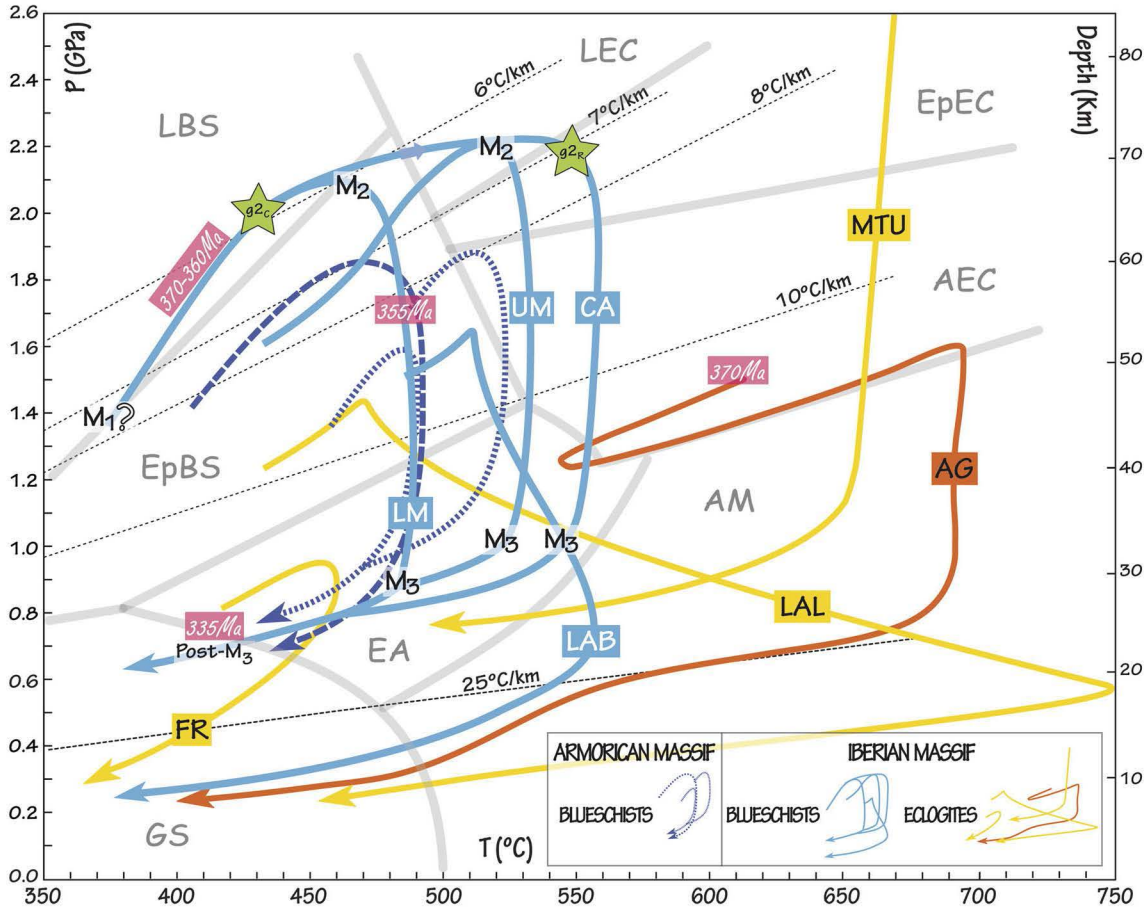

Fig. 9 *P–T* diagram showing a summary of the metamorphic paths from the lower and middle allochthonous units in the NW Iberian Massif. In the middle allochthon: the Cea´n (Cambre metabasic rocks–CA, Cea´n schists–LM and UM) and the Lamas de Abad (LAB) units. In the lower allochthon: the Malpica–Tui (MTU), Agualada (AG), Lalı´n (LAL) and Forcarei (FR) units. For comparison, the *P–T* path for the upper unit of of Ile de Groix is also shown, after Philippon et al. (2009; thickest dashed line) and Bosse et al. (2002) and Balle`vre et al. (2003; thinnest dashed line). Metamorphic facies field abbreviations *GS* greenschist facies, *EA* epidote–amphibolite facies, *AM* amphibolite facies, *LB* lawsonite blueschist facies, *EB* epidote blueschist facies, *AEC* amphibole-eclogite facies, *EpBS* and *LBS* epidote and lawsonite blueschists, respectively, *EpEc* and *LEC* epidote and lawsonite eclogites, respectively; after Heinrich and Althaus (1988), Evans (1990), Maruyama et al. (1996) and Okamoto and Maruyama (1999). M_1, M_2, M_3 and post-M_3 metamorphic events; M_2 in the CA is indicated by the stars $g2_C$ and $g2_R$ (from Fig. 9d). *g2* garnet 2, *C* core, *R* rim

geochronological data for the eclogite facies peak metamorphism in the MTC. According to U–Pb, $^{40}Ar/^{39}Ar$ and Rb–Sr data, the age of the H*P* metamorphism in eclogites and eclogite facies rocks from the MTU (i.e. lower sheet of the MTC; Fig. 1a) has been constrained at ca. 370 Ma, considered the minimum age of the subductive event that ended around ca. 365 Ma (van Calsteren et al. 1979; Santos Zalduegui et al. 1995; Rodrı´guez Aller et al. 2003; Abati et al. 2010). The $^{40}Ar/^{39}Ar$ ages presented in this study and data from Rodrı´guez Aller et al. (2003) suggest that post-peak metamorphic evolution may therefore be constrained between ca. 360 and 350 Ma, including the main stacking of the basal and middle allochthonous units. The beginning of post-nappe tectonics is defined by the intrusion of early I-type Variscan granodiorites at ca. 350–340 Ma (Serrano-Pinto et al. 1988; Bellido et al. 1992; Gallastegui 1993; unpublished data, Gutiérrez-Alonso and Fernández-Suárez pers. com.). This time interval would include the incipient partial melting related to decompression that took place under amphibolite facies conditions in the lower allochthon (Abati 2002), dated by U–Pb in zircon in the Agualada unit at ca. 346 Ma (Abati and Dunning 2002). Furthermore, it is consistent with the Lalı´n-Forcarei thrust activity constrained by Ar/39Ar40 in muscovite at around 340 Ma (Dallmeyer et al. 1997) and considered as responsible of the ultimate emplacement of the lower and middle al-lochthon nappes by the underthrusting of a new crustal sheet (the Parautochthon; Martı´nez Catala´n et al. 2002, 2007; Abati et al. 2010). Subsequently, exhumation in the MTC was driven by thrusting and recumbent folding associated with the so called Bembibre–Pico Sacro detachment system. Its activity was constrained from

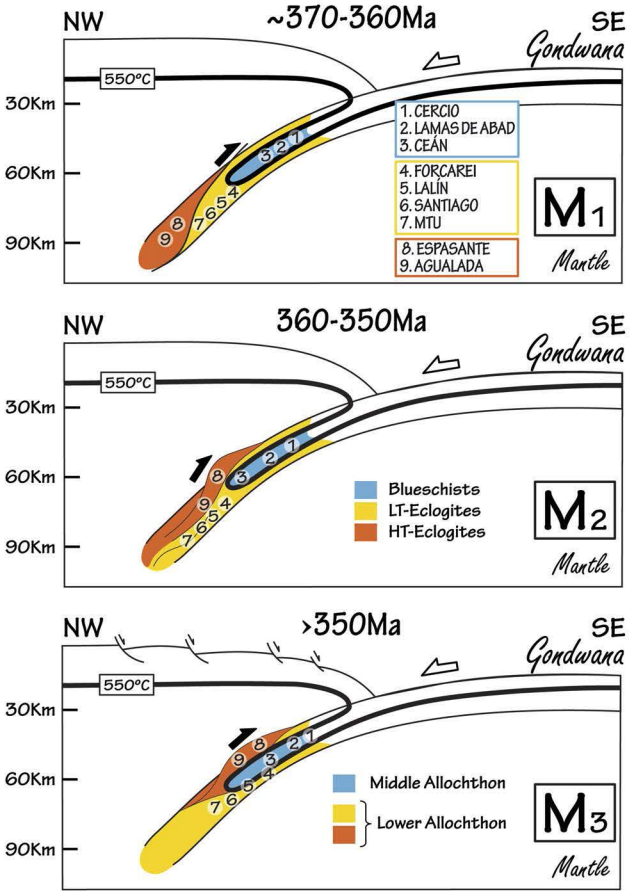

Fig. 10 Schematic cross-section of the subduction zone operating in the NW Iberian Massif at 370–360, 360–350 and below 350 Ma. Based on Martı´nez Catala´n et al. (1996) and Lo´pez-Carmona et al. (2013)

340 Ma to 317 ± 15 Ma, coeval with widespread magmatism and the late orogenic collapse (Go´mez Barreiro et al. 2007; Martı´nez Catala´n et al. 2009; D´ı ez Ferna´ndez et al. 2011), with the Bembibre–Cea´n detachment being older than the Pico Sacro detachment (Go´mez Barreiro et al. 2010). Then, the extensional shearing that led to the gravitational collapse of the orogen may be constrained at ca. 337 ± 3 Ma.

Differences between the H*P*–L*T* event (ca. 363 ± 2 Ma) and the beginning of the postnappe tectonics (at ca. 350–340 Ma) confirms that the exhumation of the MTC lasted ca. 15-20 Ma (Llana-Fu´nez and Marcos 2002; Rodrı´guez Aller et al. 2003; Abati et al. 2010). Assuming a pressure peak of 2.1 GPa (and the corresponding maximum subduction depth in the blueschists; Lo´pez-Carmona et al. 2013), a nearly isothermal decompression from 2.1 to 0.8 GPa provides an exhumation rate of ≈2.5 mm/year from 60 to 24 km. Afterwards, during the orogen collapse, a fast cooling may follow rapid exhumation because of the upward advection of heat (e.g. Ring et al. 1999). Therefore, last stages of exhumation from 0.8 to 0.5 GPa occurred within a period of ca. 15 Ma (from 350 to 335 Ma) and from $T \approx 480$ to 380 ° C, suggesting a cooling rate of 7 ° C/Ma (or a geothermal gradient of 10 ° C/km). These rates are in agreement with well-constrained natural examples and numerical thermal–mechanical models (e.g. Grasemann et al. 1999; Gerya et al. 2002; Warren et al. 2008b; Burov et al. 2014), which suggest that decom-pression occurs in two stages (1) a fast exhumation stage with little temperature change over a large depth interval and (2) a phase of fast cooling once the rocks have reached an upper crustal level (Fig. 9).

Equivalences along lower and middle allochthon in the IAA

In the Iberian Massif, according to their metamorphism and tectonostratigraphy, the lower and middle allochthons form two tectonically juxtaposed sheets (Fig. 1a). The lower allochthon is interpreted as a slice of a continental crust, where felsic orthogneisses and terrigenous metasediments predominate (Rodrı´guez Aller 2005). It forms the lower part of MTC (i.e. MTU), Santiago, Agualada, Lalı´n, Forcarei (O´ rdenes Complex) and Espasante (Cabo Ortegal Complex) units (Martı´nez Catala´n et al. 1996, 2009; Rubio Pascual et al. 2002; Rodrı´guez Aller 2005; G´o mez Barreiro et al. 2010). Possible equivalents in the South Armorican Domain are the Cellier, Saint-Mars and Mauves units (Champtoceaux Complex) and Sainte-Pazanne unit (Ess-arts Complex, Vende´e) (Balle`vre et al. in press; Fig. 1b)The middle allochthon is interpreted to represent a volcano-sedimentary sequence viewed as a more distal part of the same continental margin transitional to an oceanic domain (Rodrı´guez Aller 2005). The Cea´n (MTC), Lamas de Abad and Cercio (O´ rdenes Complex) units in the Iberian Massif (Rodrı´guez Aller et al. 2003; L´o pez-Carmona et al. 2010; G´o mez Barreiro et al. 2010), and Groix and Bois-de-Cene´ in the Armorican Massif (Balle`vre et al. 2009a, b: and references therein) belong to the middle allochthon (Balle`vre et al. in press).

In the NW Iberian Massif, both sheets share a first H*P* metamorphic event but, according to their initial location in the subducting slab, the characteristics of this metamorphism are different. In general, the lower allochthon developed eclogite facies metamorphism (Gil Ibarguchi and Ortega Girone´s 1985; Arenas et al. 1997; Rubio Pascual et al. 2002; Rodrı´guez et al. 2003), whereas the overlying middle allochthon reached blueschist facies conditions (Arenas et al. 1995; Rodrı´guez Aller et al. 2003; Lo´pez-Carmona et al. 2010; 2013). In the eastern part of the lower allochthon (Forcarei unit; Fig. 1a), the metamorphic conditions are in the blueschist facies, and going to the west, the peak *P* and *T* increases progressively up to medium-*T* eclogite facies in the MTC (Figs. 1a, 10). The

overlying middle allochthon is separated by a major tectonic contact (Bembibre–Ceán detachment) and is always in blueschist facies conditions. In a few places, the blueschist facies units are interlayered between two eclogite facies units (e.g. the Ceán Unit is sandwiched between the MTU and the Agualada unit, Fig. 1c). The interlayering was previously interpreted as an original feature of the subducted complex, related with the typical geometry of the isotherms in subduction zones (e.g. Lo´pez-Carmona et al. 2013; Fig. 10).

Acknowledgments We thank C. Valdehita from the Universidad Complutense de Madrid for her technical support and advices in $^{40}Ar/^{39}Ar$ mineral separation. We appreciate the technical assistance of D.A. Archibald and H. Fournier from the Queen's University $^{40}Ar/^{39}Ar$ Geochronology Laboratory. We are grateful to G. Gutiérrez-Alonso and J.Fernández-Suárez that kindly allow us to use their unpublished age constraints. Stimulating discussions with A. García-Casco, J.R. Martínez Catalán, M. Ballèvre and R. Arenas has considerably enriched the quality of this manuscript. We wish to thank the Executive Editor Dr. Tim Grove, Dr. Clare Warren and an anonymous referee, for their constructive comments and suggestions. This work was financially supported by the Spanish Project CGL2012-34618 (Ministerio de Economía y Competitividad) and an NSERC Discovery grant to JKWL.

References

Abati J (2002) Petrología metamórfica y geocronología de la unidad culminante del Complejo de Ordenes en la región de Carballo (Galicia, NW del Macizo Ibérico): Sada–A Coruña, vol 20. A Coruña, Ediciós do Castro, p 269

Abati J, Dunning GR (2002) Edad U-Pb en monacitas y rutilos de los paragneisses de la Unidad de Agualada (Complejo de Ordenes, NW del Macizo Ibérico). Geogaceta 32:95–98

Abati J, Gerdes A, Fernández Suárez J, Arenas R, Whitehouse MJ, Díez Fernández R (2010) Magmatism and early-Variscan continental subduction in the northern Gondwana margin recorded in zircons from the basal units of Galicia, NW Spain. Geol Soc Am Bull Bull 122:219–235

Arenas R, Rubio Pascual FJ, Diaz Garcia F, Martínez Catalán JR (1995) High-pressure micro-inclusions and development of an inverted metamorphic gradient in the Santiago Schists (Ordenes Complex, NW Iberian Massif, Spain): evidence of subduction and syncollisional decompression. J Metamorph Geol 13:141–164

Arenas R, Abati J, Martínez Catalán JR, Diaz Garcia F, Rubio Pascual FJ (1997) P–T evolution of eclogites from the Agualada Unit (Ordenes Complex, northwest Iberian Massif, Spain): implications for crustal subduction. Lithos 40:221–242

Arps CES (1981) Amphibolites and other mafic rocks of the Blastomylonitic Graben in Western Galicia, NW Spain: field relations and petrography. Leidse Geol Meded 52:57–71

Ballèvre M, Pitra P, Bohn M (2003) Lawsonite growth in the epidote blueschists from the Ile de Groix (Armorican Massif, France): a potential geobarometer. J Metamorph Geol 21:723–735

Ballèvre M, Bosse V, Ducassou C, Pitra P (2009) Palaeozoic history of the Armorican Massif: models for the tectonic evolution of the suture zones. Comptes Rendus Geosci 341:174–201

Ballèvre M, Martínez Catalán JR, López-Carmona A et al (in press) Correlation of the nappe stack in the Ibero–Armorican arc across the Bay of Biscay: a joint French–Spanish project. In: Schulmann K, Oggiano G, Lardeaux JM, Janousek V, Martínez Catalán JR, Scrivener R (eds) The variscan orogeny: extent, timescale and the formation of the European Crust. London: Geol Soc Lond Special Pub

Barrientos X, Selverstone J (1993) Infiltration vs. thermal overprinting of epidote blueschists, Ile de Groix, France. Geology 21:69–72

Bellido F, Brandle JL, Lasala M, Reyes J (1992) Consideraciones petrológicas y cronológicas sobre las rocas graníticas hercínicas de Galicia. Cuadernos del Laboratorio Xeologico de Laxe 17:241–261

Bosse V, Ballèvre M, Vidal O (2002) Ductile thrusting recorded by the garnet isograd from blueschist-facies metapelites of the Ile de Groix, Armorican Massif, France. J Petrol 43:485–510

Bosse V, Féraud G, Ballèvre M, Peucat JJ, Corsini M (2005) Rb–Sr and $^{40}Ar/^{39}Ar$ ages in blueschists from the Ile de Groix (Armorican Massif, France): implications for closure mechanisms in isotopic systems. Chem Geol 220:21–45

Burov E, Francois T, Yamato P, Wolf S (2014) Mechanism of continental subduction and exhumation of HP and UHP rocks. Gond Res 25:464–493

Clarke GL, Powell R, Fitzherbert JA (2006) The lawsonite paradox: a comparison of field evidence and mineral equilibria modelling. J Metamorph Geol 24:715–725

Dallmeyer RD, Martínez Catalán JR, Arenas R, Gil Ibarguchi JI, Gutierrez Alonso G, Farias P, Bastida F, Aller J (1997) Diachronous Variscan tectonothermal activity in the NW Iberian Massif: evidence from $^{40}Ar/^{39}Ar$ dating of regional fabrics. Tectonophysics 277:307–337

Diener JFA, Powell R (2010) Influence of ferric iron on the stability of mineral assemblages. J Metamorph Geol 28:599–613

Diener JFA, Powell R (2012) Revised activity-composition models for clinopyroxene and amphibole. J Metamorph Geol 30: 131–142

Diener JFA, Powell R, White RW (2008) Quantitative phase petrology of cordierite-orthoamphibole gneisses and related rocks. J Metamorph Geol 26:795–814

Díez Fernández R, Martínez Catalán JR, Arenas R, Abati J (2011) Tectonic evolution of a continental subduction-exhumation channel: variscan structure of the basal allochthonous units in NW Spain. Tectonics TC30:3009

Díez Fernández R, Martínez Catalán JR, Arenas R, Abati J (2012) The onset of the assembly of Pangaea in NW Iberia: constraints on the kinematics of continental subduction. Gondwana Res 22:20–25

Dipple GM, Ferry JM (1992) Fluid flow and stable isotopic alteration in rocks at elevated temperatures with applications to metamorphism. Geochim Cosmochim Acta 56:3539–3550

Dodson MH (1973) Closure temperature in geochronological and petrological systems. Contrib Mineral Petrol 40:259–274

Duprat-Oualid S, Yamato P, Pitra P (2013) Major role of shear heating on intracontinental inverted metamorphism: inference from a thermo-kinematic parametric study. Tectonophysics 608:812–831

Enami M, Suzuki K, Liou JG, Bird DK (1993) Al–Fe3+ and F–OH substitutions in titanite and constraints on their P–T dependence. Eur J Mineral 5:219–231

Engvik AK, Austrheim H, Andersen TB (2000) Structural, mineralogical and petrophysical effects on deep crustal rocks of fluid limited polymetamorphism, Western Gneiss Region, Norway. J Geol Soc Lond 157:121–134

Ernst WG (1973) Blueschists metamorphism and P–T regimes in active subduction zones. Tectonophysics 17:255–272

Evans BW (1990) Phase relations of epidote–blueschists. Lithos 25:3–23

Fleck RJ, Sutter JF, Elliot DH (1977) Interpretation of discordant $^{40}Ar/^{39}Ar$ age-spectra of Mesozoic tholeiites from Antarctica. Geochim Cosmochim Acta 41:15–32

Franz G, Spear FS (1985) Aluminious titanite (sphene) from the Eclogite zone, south-central Tauern Window, Austria. Chem Geol 50:33–46

Gallastegui G (1993) Petrología del macizo granodiorítico de Baio-Vigo (Pontevedra, España). Universidad de Oviedo, Oviedo, p 356 (unpub.)

Gerya TV, Sto¨ckhert B, Perchuk AL (2002) Exhumation of high-pressure metamorphic rocks in subduction channel: a numerical simulation. Tectonics 21. doi:10.1029/2002TC001406

Gil Ibarguchi JI, Ortega Gironés E (1985) Petrology, structure and geotectonic implications of glaucophane-bearing eclogites and related rocks fromthe Malpica–Tuy unit, Galicia, northwest Spain. Chem Geol 50:145–162

Gómez Barreiro J, Martínez Catalán JR, Arenas R, Castiñeiras P, Abati J, Díaz García F, Wijbrans JR (2007) Tectonic evolution of the upper allochthon of the Órdenes Complex (northwestern Iberian Massif): structural constraints to a polyorogenic peri-Gondwanan terrane. In: Linnemann U, Nance RD, Kraft P, Zulauf G (eds) The evolution of the Rheic Ocean: from Avalonian-Cadomian active margin to Alleghenian-Variscan collision, vol 423. Geol Soc Am Bull Special Paper, pp 315–332

Gómez Barreiro J, Martínez Catalán JR, Díez Fernández R, Arenas R, Díaz García F (2010) Upper crust reworking during gravitational collapse: the Bembibre–Pico Sacro detachment system (NW Iberia). J Geol Soc Lond 167:769–784

González Lodeiro F, Hernández Urroz J, Martínez Catalán J, Naval Balbin A, Ortega Girones E, de Pablo Macía G (1984) Santiago de Compostela. Mapa Geológico de España E 1:200000. Instituto Geológico y Minero de España, Madrid

Gottardi R, Kao PH, Saar MO, Teyssier C (2013) Effects of permeability fields on fluid, heat, and oxygen isotope transport in extensional detachment systems. Geochem Geophy Geosyst 14:1493–1522

Grasemann B, Fritz H, Vannay JC (1999) Quantitative kinematic flow analysis from the Main Central Thrust Zone (NW-Himalaya, India); implications for a decelerating strain path and the extrusion of orogenic wedges. J Struct Geol 21:837–853

Harlov D, Tropper P, Seifert W, Nijland T, Förster HJ (2006) Formation of Al-rich titanite ($CaTiSiO_4O$–$CaAlSiO_4OH$) reaction rims on ilmenite in metamorphic rocks as a function of fH_2O and fO_2. Lithos 88:72–84

Harrison T, Célérier J, Aikman A, Hermann J, Heizler J (2009) Diffusion of ^{40}Ar in muscovite. Geochim Cosmochim Acta 73:1039–1051

Heinrich W, Althaus E (1988) Experimental determination of the reactions 4 lawsonite + 1 albite = 1 paragonite + 2 zoisite + 2 quartz + 6 H_2O and 4 lawsonite + 1 jadeite = 1 paragonite + 2 zoisite + 1 quartz + 6 H_2O. Neues Jb Miner Monat 11:516–528

Holényi K, Annerstein H (1987) Iron in titanite: a Mössbauer-spectroscopy study. Can Mineral 25:429–433

Holland TJB, Powell R (1998) An internally consistent thermodynamic data set for phases of petrological interest. J Metamorph Geol 16:309–343

Holland TJB, Powell R (2003) Activity-composition relations for phases in petrological calculations: an asymmetric multicomponent formulation. Contrib Mineral Petrol 145:492–501

Holland TJB, Baker J, Powell R (1998) Mixing properties and activity-composition and relationships of chlorites in the system MgO–FeO–Al_2O_3–SiO_2–H_2O. Eur J Mineral 10:395–406

Le Bayon B, Pitra P, Ballèvre M, Bohn M (2006) Reconstructing P–T paths during continental collision using multi-stage garnet (Gran Paradiso nappe, Western Alps). J Metamorph Geol 24:477–496

Lee JKW (1995) Multipath diffusion in geochronology. Contrib Mieral Petrol 120:60–82

Liou JG (1981) Petrology of metamorphosed oceanic rocks in the Central Range of Taiwan. Mem Geol Soc China 4:291–342

Liou JG, Zhang RY, Ernst WG, Rumble D III, Maruyama S (1998) High pressure minerals from deeply subducted metamorphic rocks. In: Hemley RJ (ed) Ultrahigh-pressure mineralogy: physics and chemistry of the earth's deep interior. Rev Miner 37:33–96

Lister GS, Baldwin SL (1996) Modelling the effect of arbitrary P-T-t histories on argon diffusion in minerals using the MacArgon program for the Apple Mcintosh. Tectonophysics 253:83–109

Llana-Fúnez S (2001) La estructura de la unidad de Malpica–Tui (Cordillera varisca en Iberia). In: Serie de Tesis Doctorales 1, vol. Instituto Geológico y Minero de España, Madrid, p 295

Llana-Fúnez S, Marcos A (2002) Structural record during exhumation and emplacement of high-pressure-low-to intermediate-temperature rocks in the Malpica–Tui unit (Variscan Belt of Iberia). In: Martínez Catalán JR, Hatcher RD Jr, Arenas R, Díaz García F (eds) Variscan-Appalachian dynamics: the building of the late Paleozoic bassamen, vol 364. Geol Soc Am Bull Special Paper, pp 125–142

López-Carmona A, Abati J, Reche J (2010) Petrologic modeling of chloritoid-glaucophane schists from the NW Iberian Massif. Gondwana Res 17:377–391

López-Carmona A, Kusky TM, Santosh M, Abati J (2011) P-T and structural constraints of lawsonite and epidote blueschists from Liberty Creek and Seldovia: tectonic implications for early stages of subduction along the southern Alaska convergent margin. Lithos 121:100–116

López-Carmona A, Pitra P, Abati J (2013) Blueschist-facies metapelites from the Malpica–Tui Unit (NW Iberian Massif): phase equilibria modelling and H2O and Fe2O3 influence in high-pressure assembalges. J Metamorph Geol 31:263–280

Lyubetskaya T, Ague JJ (2009) Modeling the magnitudes and directions of regional metamorphic fluid flow in collisional orogens. J Petrol 50:1505–1531

Manon MR (2008) Heat capacity of high pressure minerals and phase equilibria of Cretan blueschists. Michigan: The University of Michigan, pp 192 (unpub.)

Martínez Catalán JR, Arenas R, Díaz García F, Rubio Pascual FJ, Abati J, Marquínez J (1996) Variscan exhumation of a subducted Paleozoic continental margin: the basal units of the Ordenes Complex, Galicia, NW Spain. Tectonics 15:106–121

Martínez Catalán JR, Díaz García F, Arenas R, Abati J et al (2002) Thrust and detachment systems in the ordenes complex (northwestern Spain): implications for the Variscan-Appalachian geodynamics. In: Martínez Catalán JR, Hatcher RD, Arenas R, Diaz Garcia F (eds) Variscan-Appalachian dynamics: the building of the late Paleozoic basement: Geol Soc Am Bull Special Paper 364:163–182

Martínez Catalán JR, Arenas R, Díaz García F et al (2007) Space and time in the tectonic evolution of the northwestern Iberian Massif: implications for the Variscan belt. Geol Soc Am Bull Mem 200:403–423

Martínez Catalán JR, Arenas R, Abati J, Sánchez Martínez S et al (2009) A rootless suture and the loss of the roots of a mountain chain: the Variscan belt of NW Iberia. Comptes Rendus Geosci 341:114–126

Maruyama S, Liou JG, Terabayashi M (1996) Blueschists and eclogites of the world and their exhumation. Int Geol Rev 38:485–594

Meinhold G (2010) Rutile and its application in earth sciences. Earth Sci Rev 102:1–28

Miller C, Satir M, Frank W (1980) High pressure metamorphism in the Tauern Window. Mitteilungen der Österreichischen Geologischen Gesellschaft 71:89–97

Newton RC, Fyfe WS (1976) High-pressure metamorphism. In: Bailey DK, Macdonald R (eds) The evolution of the crystalline rocks. Academic Press, London, pp 101–186

Okamoto K, Maruyama S (1999) The high pressure stability limits of lawsonite in the MORB + H_2O system. Am Mineral 84: 362–373

Ortega-Gutiérrez F, Solari LA, Solé J et al (2004) Polyphase, high-temperature eclogite-facies metamorphism in the Chuacus Complex, central Guatemala; petrology, geochronology, and tectonic implications. Int Geol Rev 46:445–470

Peacock SM (1987) Thermal effects of metamorphic fluids in subduction zones. Geology 15:1057–1060

Philippon M, Brun JP, Gueydan F (2009) Kinematic records of subduction and exhumation in the Ile de Groix Blueschist (Hercynian belt; Western France). J Struct Geol 31:1308–1321

Philippon M, Gueydan F, Pitra P, Brun JP (2013) Preservation of subduction-related prograde deformation in lawsonite pseudomorph-bearing rocks. J Metamorph Geol 31:571–583

Pitra P, Ballèvre M, Ruffet G (2010) Inverted metamorphic field gradient towards a Variscan suture zone (Champtoceaux Complex, Armorican Massif, France). J Metamorph Geol 28:183–208

Powell R, Holland TJB (1988) An internally consistent dataset with uncertainties and correlations: 3. Applications to geobarometry, worked examples and a computer program. J Metamorph Geol 6:173–204

Ring U, Brandon MT, Willett SD, Lister GS (1999) Exhumation processes. In: Ring U, Brandon MT, Lister GS, Willett SD (eds) Exhumation Processes: normal faulting, ductile flow and erosion. Geol Soc London Spec Publ, vol 154, pp 1–27

Rodríguez Aller J (2005) Recristalización y deformación de litologías supracorticales sometidas a metamorfismo de alta presión (Complejo de Malpica–Tui, NO del Macizo Ibérico), vol 29. O Castro, A Coruña, p 410

Rodríguez Aller J, Cosca MA, Gil Ibarguchi JI, Dallmeyer RD (2003) Strain partitioning and preservation of $^{40}Ar/^{39}Ar$ ages during Variscan exhumation of a subducted crust (Malpica–Tui complex, NW Spain). Lithos 70:111–139

Rubio Pascual FJ, Arenas R, Díaz García F, Martínez Catalán JR, Abati J (2002) Eclogites and eclogite-amphibolites from the Santiago Unit (Ordenes Complex, NW Iberian Massif, Spain): a case study of contrasting high-pressure metabasites in a context of crustal subduction. In: Martínez Catalán JR, Hatcher RD, Arenas R, Díaz García F (eds) Variscan-Appalachian dynamics: the building of the late paleozoic basement. Geol Soc Am Bull Special Paper, pp 105–124

Ruffet G, Féraud G, Ballévre M, Kiénast J (1995) Plateau ages and excess argon in phengites: an $^{40}Ar/^{39}Ar$ laser probe study of Alpine micas (Sesia Zone, Western Alps, northern Italy). Chem Geol 121:327–343

Santos Zalduegui JF, Schärer U, Gil Ibarguchi JI (1995) Isotope constraints on the age and origin of magmatism and metamorphism in the Malpica–Tuy allochthon, Galicia, NW-Spain. Chem Geol 121:91–103

Schliestedt M, Matthews A (1987) Transformation of blueschist to greenschist facies rocks as a consequence of fluid infiltration, Sifnos (Cyclades), Greece. Contrib Mineral Petrol 9:237–250

Serrano-Pinto M, Casquet C, Ibarrola E, Corretgé LG, Portugal-Ferreira M (1988) Sintese geocronológica dos granitoides do macizo hesperico. In: Bea F et al (eds) Geologia de los granitoides y rocas asociadas del macizo Hespérico. Rueda, Madrid, pp 69–86

Shelley D, Bossière G (1999) Ile de Groix: retrogression and structural developments in an extensional régime. J Struct Geol 21:1441–1445

Sherlock S, Kelley S, Inger S, Harris N, Okay A (1999) $^{40}Ar–^{39}Ar$ and Rb–Sr geochronology of high-pressure metamorphism and exhumation history of the Tavsanli Zone, NW Turkey. Contrib Mineral Petrol 137:46–58

Smye AJ, Greenwood LV, Holland TJB (2010) Garnet-chloritoid-kyanite assemblages: eclogite facies indicators of subduction constraints in orogenic belts. J Metamorph Geol 28:753–768

Souche A, Medvedev S, Andersen TB, Dabrowski M (2013) Shear heating in extensional detachments: implications for the thermal history of the Devonian basins of W Norway. Tectonophysics. doi:10.1016/j.tecto.2013.07.005

Stober I, Bucher K (2004) Fluid sinks within the earth's crust. Geofluids 4:143–151

Stu¨we K (1997) Effective bulk composition changes due to cooling: a model predicting complexities in retrograde reaction textures. Contrib Mineral Petrol 129:43–52

Tinkham DK, Zuluaga CA, Stowell HH (2003) Metapelite phase equilibria modelling in MnNCKFMASH: the effect of variable Al2O3 and MgO/(MgO + FeO) on mineral stability. Am Mineral 88:1174

Tracy RJ (1982) Compositional zoning and inclusions in metamorphic minerals. In: Ferry JM (ed) Characterization of metamorphism through mineral equilibria. Mineralogical Society of America, Washington, pp 355–397

Tropper P, Manning CE, Essene EJ (2002) The substitution of Al and F in titanite at high pressure and temperature: experimental constraints on phase relations and solid solution properties. J Petrol 43:1787–1814

Van Calsteren PWC, Boblrijk NAIM, Hereda EH et al (1979) Isotopic dating of older elements (including the Cabo Ortegal mafic-ultramafic complex) in the Hercynian Origen of NW Spain: manifestations of a presumed Early Paleozoic mantle-plume. Chem Geol 24:35–56

Vega-Granillo R, Talavera-Mendoza O, Meza-Figueroa D et al (2007) Pressure–temperature–time evolution of Paleozoic high-pressure rocks of the Acatla´n Complex (southern Mexico): implications for the evolution of the Iapetus and Rheic Oceans. Geol Soc Am Bull Bull 119:1249–1264

Villa JE, Hermann IM, Mu¨ntener O, Trommsdorff V (2000) ^{40}Ar-^{39}Ar dating of multiply zoned amphibole generations (Malenco, Italian Alps). Contrib Mineral Petrol 140:363–381

Walker JD, Geissman JW, Bowring SA, Babcock LE, compilers (2012) Geologic time scale v. 4.0: Geol Soc Am Bull doi:10.1130/2012.CTS004R3C

Warren CJ, Beaumont C, Jamieson RA (2008a) Deep subduction and rapid exhumation: role of crustal strength and strain weakening in continental subduction and ultrahigh-pressure rock exhumation. Tectonics 27:TC6002

Warren CJ, Beaumont C, Jamieson RA (2008b) Modelling tectonic styles and ultrahigh pressure (UHP) rock exhumation during the transition from oceanic subduction to continental collision. Earth Planet Sci 267:129–145

Warren C, Sherlock S, Kelley S (2010) Interpreting high-pressure phengite $^{40}Ar/^{39}Ar$ laserprobe ages: an example from Saih Hatat, NE Oman. Contrib Mineral Petrol 161:991–1009

Warren CJ, Hanke F, Kelley SP (2012) When can muscovite 40Ar/39Ar dating constrain the timing of metamorphic exhumation? Chem Geol 291:79–86

Wheeler J (1996) DIFFARG: a program for simulating argon diffusion profiles in minerals. Comput Geosci 22:919–929

White RW, Powell R, Holland TJB, Worley B (2000) The effect of TiO_2 and Fe_2O_3 on metapelitic assemblages at greenschist and amphibolite facies conditions: mineral equilibria calculations in the system K_2O–FeO–MgO–Al_2O_3–SiO_2–H_2O–TiO_2–Fe_2O_3. J Metamorph Geol 18:497–511

White RW, Powell R, Holland TJB (2007) Progress relating to calculation of partial melting equilibria for metapelites. J Metamorph Geol 25:511–527

Will T, Okrusch M, Schmädicke E, Chen G (1998) Phase relations in the greenschist-blueschist-amphibolite-eclogite facies in the system Na_2O–CaO–FeO–MgO–Al_2O_3–SiO_2–H_2O (NCFMASH), with application to metamorphic rocks from Samos, Greece. Contrib Mineral Petrol 132:85–102

Wing BA, Ferry JM (2002) Three-dimensional geometry of metamorphic fluid flow during Barrovian regional metamorphism from an inversion of combined petrologic and stable isotope data. Geology 30:639–642

Zuluaga CA, Stowell HH, Tinkham DK (2005) The effect of zoned garnet on metapelite pseudosection topology and calculated-metamorphic P-T paths. Am Mineral 90:1619–1628